Metabolic Engineering 74 (2022) 83–97

Contents lists available at ScienceDirect

Metabolic Engineering

journal homepage: www.elsevier.com/locate/meteng

A synthetic C2 auxotroph of *Pseudomonas putida* for evolutionary engineering of alternative sugar catabolic routes

Nicolas T. Wirth [a], Nicolás Gurdo [a], Nicolas Krink [a], Àngela Vidal-Verdú [b], Stefano Donati [a], Lorena Férnandez-Cabezón [a], Tune Wulff [a], Pablo I. Nikel [a,*,1]

[a] The Novo Nordisk Foundation Center for Biosustainability, Technical University of Denmark, Kemitorvet, 220 2800, Kongens Lyngby, Denmark
[b] Institute for Integrative Systems Biology I2SysBio (Universitat de València-CSIC), Calle del Catedràtic Agustin Escardino Benlloch 9, 46980, Paterna, Spain

ARTICLE INFO

Keywords:
Metabolic engineering
Pseudomonas putida
Synthetic biology
Synthetic metabolism
Synthetic auxotrophy
Phosphoketolase
Adaptive laboratory evolution

ABSTRACT

Acetyl-coenzyme A (AcCoA) is a metabolic hub in virtually all living cells, serving as both a key precursor of essential biomass components and a metabolic sink for catabolic pathways for a large variety of substrates. Owing to this dual role, tight growth-production coupling schemes can be implemented around the AcCoA node. Building on this concept, a synthetic C2 auxotrophy was implemented in the platform bacterium *Pseudomonas putida* through an *in silico*-informed engineering approach. A growth-coupling strategy, driven by AcCoA demand, allowed for direct selection of an alternative sugar assimilation route—the phosphoketolase (PKT) shunt from bifidobacteria. Adaptive laboratory evolution forced the synthetic *P. putida* auxotroph to rewire its metabolic network to restore C2 prototrophy *via* the PKT shunt. Large-scale structural chromosome rearrangements were identified as possible mechanisms for adjusting the network-wide proteome profile, resulting in improved PKT-dependent growth phenotypes. ^{13}C-based metabolic flux analysis revealed an even split between the native Entner-Doudoroff pathway and the synthetic PKT bypass for glucose processing, leading to enhanced carbon conservation. These results demonstrate that the *P. putida* metabolism can be radically rewired to incorporate a synthetic C2 metabolism, creating novel network connectivities and highlighting the importance of unconventional engineering strategies to support efficient microbial production.

1. Introduction

Acetyl-coenzyme A (AcCoA) is a key component in the metabolism of virtually all living organisms (Lu et al., 2019; Shi and Tu, 2015). The thioester is a metabolite hub and the entry point to the tricarboxylic acid (TCA) cycle, in which most of the ATP-generating reducing equivalents are produced. AcCoA also plays a central role in biochemical pathways leading to essential biomass constituents, e.g., amino acids, cell wall components (acetylated amino sugars), fatty acids (Vadali et al., 2004), and multiple compounds of industrial interest (i.e., polyketides, isoprenoids, alcohols, and polyhydroxyalkanoates) can be produced from AcCoA (Gambacorta et al., 2020; Mezzina et al., 2021; Wang et al., 2022; Yang et al., 2020; Zhu et al., 2022). Conversely, various catabolic pathways for a broad spectrum of compounds form a 'funnel' ultimately converging at the AcCoA node (Weimer et al., 2020). Given its central role as a biomass precursor, the pivotal AcCoA node can be harnessed for constructing synthetic pathways where both product formation and consumption are tightly coupled to growth—provided that they represent the only AcCoA source in a suitable selection strain.

Having adapted to frequent periods of carbon starvation, the metabolism of soil generalist microbes (e.g., *Pseudomonas putida*) is optimized for the utilization of a wide variety of substrates without producing overflow metabolites (Belda et al., 2016; Ebert et al., 2011; Poblete-Castro et al., 2012). The intracellular AcCoA concentration—and its relative levels compared to non-esterified CoA—is maintained at low levels in *P. putida* regardless of the metabolic status (Kozaeva et al., 2021), in contrast to most facultatively anaerobic bacteria (Chang et al., 1999; Chohnan et al., 1997). In bacteria displaying the two most prevalent glycolytic routes, the Embden-Meyerhof-Parnas (EMP) and the Entner-Doudoroff (ED) pathway (Volke et al., 2021), AcCoA is almost exclusively formed through pyruvate (Pyr) oxidation (Bar-Even et al., 2012; Chavarría et al., 2013; Nikel et al., 2016a,b). This reaction,

* Corresponding author. The Novo Nordisk Foundation Center for Biosustainability, Technical University of Denmark, Kemitorvet, 220 2800, Kgs. Lyngby, Denmark.
E-mail address: pabnik@biosustain.dtu.dk (P.I. Nikel).
[1] Lead contact

https://doi.org/10.1016/j.ymben.2022.09.004
Received 22 July 2022; Received in revised form 17 September 2022; Accepted 17 September 2022
Available online 23 September 2022

catalyzed by the Pyr dehydrogenase complex (PDHc), involves substrate decarboxylation and consequently leads to net carbon loss (Patel et al., 2014). In contrast, the phosphoketolase (PKT) pathway, originally described in heterolactic fermentative bacteria (Scardovi and Trovatelli, 1965), constitutes an alternative glycolytic route that provides AcCoA without CO2 release. PKTs form a unique class of enzymes, closely related to transketolase (EC 2.2.1.1)—an essential component of the pentose phosphate (PP) pathway (Krüsemann et al., 2018). They require thiamine diphosphate and divalent metal ions as cofactors, catalyzing the cleavage of xylulose-5-phosphate (Xu5P) or fructose-6-phosphate (F6P) to acetyl-phosphate (Ac–P) and glyceraldehyde-3-phosphate (G3P) or erythrose-4-phosphate (E4P), respectively. The enzymatic reaction involves ketol cleavage, dehydration, and phosphorolysis in a single step (Tittmann, 2014). Ac–P can be converted into AcCoA *via* phosphate acetyltransferase (Pta), allowing for the direct conversion of sugar phosphates into AcCoA without carbon loss (Bogorad et al., 2013). Streamlining sugar utilization through this carbon-conserving pathway has the potential of increasing maximum theoretical yields for AcCoA-derived products in biotechnological applications (Hellgren et al., 2020; Henard et al., 2015; Ku et al., 2020; Orsi et al., 2022). Such a strategy has been harnessed both in bacteria and yeast, most often as an additional route to the linear EMP glycolysis (Liu et al., 2019; Lu et al., 2019; Qin et al., 2020; Wang et al., 2019). The question is whether a synthetic PKT metabolism can be implanted in *P. putida* to boost AcCoA levels. Such a goal entails a radical rewiring of the metabolic connections that lead to AcCoA formation in this obligate aerobe (Nikel and de Lorenzo, 2013) that runs a cyclic, ED-based sugar catabolism (Nikel et al., 2015, 2021; Volke and Nikel, 2018).

The inherent complexity of metabolic systems poses an obstacle when deliberately modifying core traits, yet adaptive laboratory evolution (ALE) aids in improving the performance of whole-cell biocatalysts for specific biochemical tasks (Fernández-Cabezón et al., 2019; Sandberg et al., 2019). A requisite for evolutionary engineering approaches is that the desired property can be subject to a selection pressure that couples an improved catalytic performance with a fitness gain—e.g., by creating a metabolic deficiency in selection strains (Cros et al., 2022; Orsi et al., 2021; Wenk et al., 2018). Building on these concepts, in this study we adopted *in silico* modeling to identify key reactions involved in AcCoA turnover in *P. putida*, and a synthetic two-carbon (C2) auxotrophy was established by systematically eliminating all of the AcCoA-forming reactions. As proof-of-principle of C2-based selection schemes, an artificial PKT pathway was implemented in the rewired *P. putida* strain, and ALE was applied to optimize the synthetic metabolism. Multi-omic characterization of the resulting strains, which included functional genomics, targeted proteomics, and ^{13}C-based fluxomics, showed that network-wide adaptations enabled carbon conservation in evolved clones—evidenced by a ca. 80% reduction in CO_2 formation in bioreactor batch cultures. Taken together, our results demonstrate the suitability of establishing alternative routes for sugar catabolism in *P. putida*, supported by *in silico*-predicted metabolic rewiring and evolutionary engineering, thus paving the way towards carbon-efficient bioproduction.

2. Materials and methods

2.1. Bacterial strains and culture conditions

The bacterial strains employed in this study are listed in Table 1. *E. coli* and *P. putida* were incubated at 37 °C and 30 °C, respectively. For propagation and storage, routine cloning procedures, and during genome engineering manipulations, cells were grown in lysogeny broth (LB) medium (10 g L^{-1} tryptone, 5 g L^{-1} yeast extract, and 10 g L^{-1} NaCl). Liquid cultures were performed using either 50-mL centrifuge tubes with a medium volume of 5–10 mL, or in 500-mL Erlenmeyer flasks covered with cellulose plugs (Carl Roth, Karlsruhe, Germany) containing a medium volume of 50 mL. All liquid cultures were agitated at 250 rpm (in a MaxQ™8000 incubator; ThermoFisher Scientific, Waltham, MA, USA). Solid culture media contained 15 g L^{-1} agar. Selection of plasmid-harboring cells was achieved by adding kanamycin (Km), gentamicin (Gm), or streptomycin (Sm) to the culture media at 50 μg mL^{-1}, 10 μg mL^{-1}, and 50 μg mL^{-1}, respectively.

For phenotypic characterizations in microtiter plates as well as in shaken-flask cultivations, experiments were performed in de Bont minimal (DBM) medium (Hartmans et al., 1989) additionally buffered with 5 g L^{-1} 3-(*N*-morpholino)propane sulfonic acid (MOPS) at pH = 7.0 and supplemented with different carbon compounds as explained in the text. Before launching plate reader experiments (for 96-well plates: ELx808, BioTek Instruments; Winooski, VT, USA; and for 24-well plates: Synergy

Table 1
Bacterial strains used in this study.

Strain	Relevant characteristics	Reference or source
Escherichia coli		
DH5α λ*pir*	Cloning host; F^- λ^- *endA1 glnX44*(AS) *thiE1 recA1 relA1 spoT1 gyrA96*(Nal^R) *rfbC1 deoR nupG* Φ80(*lacZ*Δ*M15*) Δ(*argF-lac*)*U169 hsdR17* ($r_K^- m_K^+$), λ*pir* lysogen	Platt et al. (2000)
Pseudomonas putida		
KT2440	Wild-type strain, derived from *P. putida* mt-2 (Worsey and Williams, 1975) cured of the TOL plasmid pWW0	Bagdasarian et al. (1981)
SCA1	As KT2440, Δ*aceEF*	This work
SCA3	As KT2440, Δ*bkdAA* Δ*ltaE* Δ*aceEF*	This work
$SCA8_{PD}$	As KT2440, Δ*bkdAA* Δ*pcaBDC* Δ*paaEDCBA* Δ*davBA* Δ*gabT* Δ*glcB* Δ*hmgABC*[a] Δ*mmsA2*	This work
SCA9	As KT2440, Δ*bkdAA* Δ*pcaBDC* Δ*paaEDCBA* Δ*davBA* Δ*gabT* Δ*glcB* Δ*hmgABC*[a] Δ*mmsA2* Δ*aceEF*	This work
$SCA14_{PD}$	As KT2440, Δ*bkdAA* Δ*ltaE* Δ*pcaBDC* Δ*paaEDCBA* Δ*davBA* Δ*gabT* Δ*glcB* Δ*hmgABC*[a] Δ*eutBC* Δ*mmsA2* Δ*mmsA1* Δ*acoABC* Δ*prpC* Δ*benABCD*[b]	This work
SCA15	As KT2440, Δ*bkdAA* Δ*ltaE* Δ*pcaBDC* Δ*paaEDCBA* Δ*davBA* Δ*gabT* Δ*glcB* Δ*hmgABC*[a] Δ*eutBC* Δ*mmsA2* Δ*mmsA1* Δ*acoABC* Δ*prpC* Δ*benABCD*[b] Δ*aceEF*	This work
SCA18	As KT2440, Δ*bkdAA* Δ*ltaE* Δ*pcaBDC* Δ*paaEDCBA* Δ*davBA* Δ*gabT* Δ*glcB* Δ*hmgABC*[a] Δ*eutBC* Δ*mmsA2* Δ*mmsA1* Δ*acoABC* Δ*prpC* Δ*benABCD*[b] Δ*aceEF* Δ*glpR* Δ*gltA* Δ*crc*	This work
$SCA3_{PK}$	As KT2440, Δ*bkdAA* Δ*ltaE* Δ*aceEF* LP::$xfpk^{Ba}$; *P. putida* SCA3 with *B. adolescentis xfpk* chromosomally integrated into a landing pad (LP) between *PP_0013* and *PP_5421*	This work
$SCA3_{PK\text{-}Tn}$	As KT2440, Δ*bkdAA* Δ*ltaE* Δ*aceEF* LP::$xfpk^{Ba}$ *att*Tn*7*::*gntZ-rpe*; strain $SCA3_{PK}$ with the translationally-coupled *gntZ* and *rpe* genes chromosomally integrated at the unique *att*Tn*7* site	This work
$evoSCA3_{PK\text{-}Tn}$_A	Evolved variant of $SCA3_{PK\text{-}Tn}$ harboring the 94,691-bp deletion Δ(*PP_2985-PP_3088*) and inversion INV(*PP_2964-PP_5547*), as well as a single G→A point mutation in *tilS* (*PP_1608*)	This work
$evoSCA3_{PK\text{-}Tn}$_B	Evolved variant of $SCA3_{PK\text{-}Tn}$, same as $evoSCA3_{PK\text{-}Tn}$_A, but harboring only the point mutation in *tilS*	This work

[a] The Δ*hmgABC* deletion causes the formation of a brown pigment when cells are grown in LB medium, indicating homogentisic acid accumulation that, upon oxidation to a quinoid derivative, polymerizes spontaneously and generates melanic compounds (Arias-Barrau et al., 2004).
[b] The *benABCD* operon was removed to avoid degradation of the inducer 3-methylbenzoate and the associated browning of culture media (Volke et al., 2020b).

H1, BioTek Instruments) with SCA strains and varying carbon sources, cells were pre-grown in LB medium. For all other experiments, the pre-culture media were identical to those used for the experiment unless otherwise indicated. The precultures were harvested by centrifugation at 8000×*g* for 2 min, washed with DBM medium without any carbon substrate, and resuspended in the final media at the desired starting optical density measured at 600 nm (OD_{600}). Cell growth was monitored by measuring the OD_{600} over time. ALE of strains was performed in 24-well deep-well plates covered with a Sandwich Cover (PreSens Precision Sensing, Regensburg, Germany) and filled with 2 mL of DBM medium (containing an appropriate carbon substrate) per well; other ALE conditions are described below.

2.2. Cloning procedures and plasmid construction

All plasmids used in this work are listed in Table 2. Oligonucleotides used for the PCR-amplification of fragments and genotyping *via* colony PCR are listed in Table S1 in **Additional File 1**. Uracil-excision (*USER*) cloning (Cavaleiro et al., 2015) was used for constructing all plasmids. The AMUSER tool was employed for oligonucleotide design (Genee et al., 2015). All genetic manipulations followed protocols described previously (Nikel et al., 2016b; Volke et al., 2020a,b; Wirth et al., 2020; Wirth and Nikel, 2021). DNA fragments employed in assembly reactions were amplified using Phusion™ *U* high-fidelity DNA polymerase (Thermo Fisher Scientific, Waltham, Massachusetts, USA) according to the manufacturer's specifications. The identity and correctness of all plasmids and DNA constructs were confirmed by Sanger sequencing (Eurofins Genomics, Ebersberg, Germany). For genotyping experiments after cloning procedures and genome manipulations, colony PCRs were performed using the commercial *OneTaq*™ master mix (New England BioLabs; Ipswich, MA, USA) according to the manufacturer's instructions. *E. coli* DH5α *λpir* was employed for cloning. Chemically-competent *E. coli* cells were prepared and transformed with plasmids according to well-established protocols (Calero et al., 2020; Sambrook and Russell, 2001); *P. putida* was rendered electro-competent following the method by Choi et al. (2006).

2.3. Genome-scale metabolic model (GSMM) simulations

The most recent genome-scale metabolic network reconstruction for *P. putida* KT2440, *i*JN1463 (Nogales et al., 2020), was subjected to flux balance analysis [FBA (Orth et al., 2010)] within the COBRApy toolbox (Ebrahim et al., 2013) to predict optimal flux distributions and to identify reactions contributing to AcCoA turnover. Glucose uptake rate and ATP maintenance requirement were fixed at 6.3 mmol g cell dry weight $(CDW)^{-1}$ h^{-1} and 0.92 mmol g_{CDW}^{-1} h^{-1} [experimentally determined by del Castillo et al. (2007) and Ebert et al. (2011), respectively]. After an initial deletion of the PDHc reaction, the following steps were iterated to identify potential alternative AcCoA sources (reaction loops were not permitted): (i) optimizing flux distribution for biomass formation; (ii) identifying AcCoA-forming reaction with the highest flux under the current distribution; (iii) tracing fluxes leading to AcCoA to pinpoint the metabolic pathway(s) involved therein; and (iv) removing the entry reaction of the pathway, simultaneously avoiding the creation of auxotrophies. The identified pathways were then analyzed regarding the flux towards the first biomass constituent in the AcCoA-generating pathway and ranked according to their value within the flux distribution of the wild-type model. This ranking was used to inform a hierarchy of gene deletions to be established in *P. putida* to create a family of synthetic C2 auxotrophic strains.

2.4. Targeted proteomics assisted by mass spectrometry

P. putida strains were pre-cultured overnight in DBM medium supplemented with 30 mM glucose or 30 mM glucose and 30 mM acetate; cultures with identical media were inoculated at an initial OD_{600} of 0.05. Samples were taken in the mid-exponential phase, and cells were harvested by centrifugation at 17,000×*g* for 2 min at 4 °C. After removal of

Table 2
Plasmids used in this study.

Plasmid name	Relevant characteristics[a]	Source or reference
pGNW2	Suicide vector used for genetic manipulations in Gram-negative bacteria; *oriT, traJ, lacZα, ori*(R6K), P_{14g}*(BCD2)→msfGFP*; Km^R	Wirth et al. (2020)
pSNW2	Derivative of vector pGNW2 with the translation initiation sequence of *msfGFP* replaced by the very strong translational coupling sequence *BCD2*	Volke et al. (2020b)
pQURE6·H	Conditionally-replicating vector; derivative of vector pJBSD1 carrying XylS/*Pm→I-SceI* and *P14g(BCD2)→mRFP*; Gm^R	Volke et al. (2020b)
pSNW2•Δ*aceEF*	Derivative of pGNW2 carrying HAs to delete *aceEF* in *P. putida* KT2440	This study
pSNW2•Δ*gltA*	Derivative of pGNW2 carrying HAs to delete *gltA* in *P. putida* KT2440	This study
pSNW2•Δ*acoABC*	Derivative of pGNW2 carrying HAs to delete *acoABC* in *P. putida* KT2440	This study
pSNW2•Δ*amaC-dpkA*	Derivative of pGNW2 carrying HAs to delete *amaC-dpkA* in *P. putida* KT2440	This study
pSNW2•Δ*bkdAA*	Derivative of pGNW2 carrying HAs to delete *bkdAA* in *P. putida* KT2440	This study
pSNW2•Δ*crc*	Derivative of pGNW2 carrying HAs to delete *crc* in *P. putida* KT2440	This study
pSNW2•Δ*davBA*	Derivative of pGNW2 carrying HAs to delete *davBA* in *P. putida* KT2440	This study
pSNW2•Δ*eutBC*	Derivative of pGNW2 carrying HAs to delete *eutBC* in *P. putida* KT2440	This study
pSNW2•Δ*gabT*	Derivative of pGNW2 carrying HAs to delete *gabT* in *P. putida* KT2440	This study
pSNW2•Δ*glcB*	Derivative of pGNW2 carrying HAs to delete *glcB* in *P. putida* KT2440	This study
pSNW2•Δ*hmgABC*	Derivative of pGNW2 carrying HAs to delete *hmgABC* in *P. putida* KT2440	This study
pSNW2•Δ*ltaE*	Derivative of pGNW2 carrying HAs to delete *ltaE* in *P. putida* KT2440	This study
pSNW2•Δ*mmsA1*	Derivative of pGNW2 carrying HAs to delete *mmsA1* in *P. putida* KT2440	This study
pSNW2•Δ*mmsA2*	Derivative of pGNW2 carrying HAs to delete *mmsA2* in *P. putida* KT2440	This study
pSNW2•Δ*paaEDCBA*	Derivative of pGNW2 carrying HAs to delete *paaEDCBA* in *P. putida* KT2440	This study
pSNW2•Δ*pcaBDC*	Derivative of pGNW2 carrying HAs to delete *pcaBDC* in *P. putida* KT2440	This study
pSNW2•Δ*prpC*	Derivative of pGNW2 carrying HAs to delete *prpC* in *P. putida* KT2440	This study
pTn7-M	Tn*7* integration vector; *ori*(R6K); Km^R, Gm^R	Choi et al. (2005)
pTn7•P_{14g}*(BCD10)→gntZ-rpe*	Derivative of pTn7-M used for chromosomal integration of a synthetic *gntZ-rpe* operon under the control of a P_{14g}*(BCD10)* element. The two genes within the synthetic operon were translationally coupled by overlapping the *STOP* codon (in bold) of *gntZ* and the *START* codon of *rpe* (underlined), i.e., **ATG**A	This study
pTNS2	Helper plasmid constitutively expressing the *tnsABCD* genes encoding the Tn*7* transposase; *oriV*(R6K); Amp^R	Choi and Schweizer (2006)
pSEVA438	Standard expression vector; *oriV(pBBR1)*, Sm^R; XylS/*Pm*	Martínez-García et al. (2019)
pS438•pta^{Ec}	Expression vector derivative of pSEVA438; *oriV(pBBR1)*, Sm^R; XylS/*Pm→*pta^{Ec}	This work

[a] Antibiotic markers: *Amp*, ampicillin; *Km*, kanamycin; *Gm*, gentamicin; and *Sm*, streptomycin. *HA*, homology arms.

the supernatant, cell pellets were frozen and kept at −80 °C until proteomic analysis was performed as described previously (Rennig et al., 2019). To assign the detected peptides to their functions, a protein database consisting of the *P. putida* reference proteome [UP000000556 (Belda et al., 2016)] was used, supplemented with heterologously expressed proteins.

2.5. Statistical analysis of proteomic data

Proteomic data, acquired as described above, were analyzed using a customized R script in RStudio (version 2021.09.2). First, entries with missing values were filtered to retain only those proteins that had been detected in every replicate of at least one condition. The abundance values were $\log_2$-transformed and normalized *via* variance stabilization normalization using the *vsn* package (Huber et al., 2002). Next, missing values were imputed *via* random draws from a left-shifted distribution ["MinProb" method in the *MSnbase* package with a q value of 0.01 (Gatto et al., 2021)]. A differential enrichment test was performed for each contrast in the dataset based on protein-wise linear models and empirical Bayes statistics using *limma* (Ritchie et al., 2015). *P*-values were adjusted using *fdrtool* with the Benjamini-Hochberg method (Strimmer, 2008); the adjusted *P*-value threshold for significant observations was set at a value of 0.05. Volcano plots were generated with the *ggplot2* package. The *pheatmap* package was used to create heatmaps of protein abundances within all samples. Enrichment analysis of KEGG pathways (Qiu, 2013) was performed using the *clusterProfiler* package (Wu et al., 2021), with all genes listed for *P. putida* KT2440 as background 'universe' and a *P*-value threshold of 0.1.

2.6. Adaptive laboratory evolution

Evolution was performed in 24-well deep-well plates filled with 2 mL of DBM medium supplemented with 30 mM glucose and 0.5 mM 3-methylbenzoate (3-*m*Bz). ALE was performed in a single evolutionary line for each of the *P. putida* strains indicated in the text. A volume of 50 µL (from glucose cultures) or 20 µL (from cultivation steps in the presence of glucose and acetate) of each well was passed into fresh medium every other day. For every second passage, the medium contained an additional 20 mM of potassium acetate to recover biomass at higher concentrations. After 1 month of cultivation under these conditions, ALE was continued using DBM supplemented only with glucose.

2.7. Bioreactor fermentations

The batch fermentations were performed in BIOSTAT™ Qplus 1-L bioreactors (Sartorius, Göttingen, Germany) with a working culture volume of 800 mL. Precultures were grown overnight in 500-mL Erlenmeyer flasks filled with 10% (v/v) DBM medium supplemented with 5 g L^{-1} MOPS and 30 mM glucose. The same medium was used in the bioreactor runs. Precultures were harvested by centrifugation at 4000×*g* for 10 min and resuspended in fresh culture medium (with no carbon substrate added) to inoculate the bioreactors. Aeration of the vessels was achieved *via* horseshoe-shaped spargers with ambient air at a flow rate of 0.824 L min^{-1}. The dissolved oxygen concentration (dO_2) was measured online using an oxygen electrode and kept above 40% of saturation by increasing the stirring speed from 500 to 1000 rpm. The lower stirring speed threshold was reduced to 250 rpm after 5.5 h to reduce shear stress on the cells and to prevent biofilm formation. Sigma-Aldrich Co. antifoam 204 reagent (St. Louis, Missouri, USA) was added when required to reduce foaming in cultivations of strain KT2440. The cultures were maintained at 30 °C and pH = 7.0 by online measurements with standard thermometers and pH electrodes and the automatic addition of 7 M NaOH. The composition of the off-gas was analyzed online with a Prima BT Bench Top Process mass spectrometer (Thermo Fisher Scientific).

Physiological parameters for *P. putida* KT2440 and strain $SCA3_{PK\text{-}Tn}$/pS438•pta^{Ec} were obtained as follows: cell growth was followed *via* OD_{600} measurements and, for strain KT2440, CDW determinations were carried out with a Moisture analyzer WBA-110M (Witeg Labortechnik, Wertheim, Germany). CDW values were derived from OD_{600} measurements by applying correlation factors obtained from standard curves with the OD_{600} values and CDW determinations for each strain. Specific growth rates (µ) were determined as described below. Biomass yields on glucose $Y_{X/S}$ (or the sum of all six-carbon moieties) were obtained as the slope of linear correlations of biomass ($g_{CDW}\,L^{-1}$)-over-substrate ($g_S\,L^{-1}$) plots. CO_2 production was calculated from the CO_2 content in the in-gas and the off-gas; dissolved inorganic carbon species (carbonate and CO_2) were neglected. The C-mol amount in biomass was derived from the CDW and the elemental biomass composition of *P. putida* KT2440 (van Duuren et al., 2013).

2.8. ^{13}C-Labeling experiments

For parallel isotopic tracer experiments, *P. putida* KT2440 and strain $SCA3_{PK\text{-}Tn}$/pS438•pta^{Ec} were grown as indicated in section *2.1* by supplementing the medium with the corresponding labeled substrate. Three isotopic tracers were used: (i) 99% [3–$^{13}C_1$]-glucose, (ii) 99% [4–$^{13}C_1$]-glucose, and (iii) a 50%:50% mixture of naturally labeled ^{12}C- and 99% (w/w) [$^{13}C_6$]-glucose. All labeled substrates were purchased from Cambridge Isotope Laboratories Inc. (Teddington, Middlesex, United Kingdom). Before tracer experiments, cells were streaked from a cryostock onto an LB agar plate and grown overnight for 18 h. Pre-cultures were performed in 12-mL plastic tubes containing 3 mL of DBM medium (with the respective labeled carbon sources), using a single colony per biological replicate from the plate. The pre-cultures were incubated at 250 rpm in an orbital shaker at 30 °C. The cultures were inoculated at an initial OD_{600} of 0.05 in a 100-mL Erlenmeyer flask containing 20 mL of DBM medium with the specific tracer. Aliquots were taken from the pre-cultures, centrifuged at 10,000×*g* and 4 °C for 5 min, and washed twice using DBM medium without a carbon source. All experiments were performed in three biological replicates and two technical replicates, and multiple samples were harvested for the analysis of either proteinogenic amino acids or cellular sugars. Sample preparation and GC-MS analysis of proteinogenic amino acids was performed as described previously (Kutuzova et al., 2020). For analysis of cellular sugars, sample preparation was performed as described previously (Kohlstedt and Wittmann, 2019) and samples were analyzed with the same GC-MS method used for amino acids analysis.

2.9. Reaction network and computational design for flux estimation

The metabolic networks of *P. putida* KT2440 and strain $SCA3_{PK\text{-}Tn}$/pS438•pta^{Ec} were built based on the most updated genome-scale metabolic model (Nogales et al., 2020). In total, 84 reactions were included as part of the central carbon metabolism in *P. putida* KT2440. In the case of strain $SCA3_{PK\text{-}Tn}$/pS438•pta^{Ec}, three additional reactions were added: (i) F6P to Ac–P and E4P, (ii) Xu5P to Ac–P and G3P [(i) and (ii) are the two possible reactions catalyzed by PKT], and (iii) Ac–P to AcCoA. All included reactions, as well as the carbon atom transitions, are listed in **Additional File 2**. The INCA software package was utilized for ^{13}C-metabolic flux analysis (^{13}C-MFA; Young, 2014). Specific growth rates, and uptake or secretion rates for glucose, gluconate, 2-ketogluconate (2KG), and Pyr were used to constrain the MFA model. The biomass equation was derived from the normalized precursor drainage to calculate experimental growth rates (Kohlstedt and Wittmann, 2019). The relative intracellular fluxes (expressed as a percentage of the q_S) were estimated by iteratively minimizing the weighted sum-of-squared-residuals (SSR) between simulated and experimental labeling data for proteinogenic amino acids, extracellular sugars and sugar acids, glycogen, and glucosamine [i.e., the mass isotopomer distribution vectors (MDVs) of all analyzed fragments (Crown and Antoniewicz, 2012)]. The data used for ^{13}C-MFA is available in **Additional**

File 2. To ensure that the global best solution was determined, the flux estimation was repeated at least 20 times, starting with random initial values. Upon convergence, a χ^2 test was applied to test the goodness-of-fit, and accurate 95% confidence intervals were calculated by determining the sensitivity of the sum of squared residuals to flux parameter variations (Antoniewicz et al., 2006). The complete set of flux results, including best fits, standard deviations, as well as upper and lower bounds of the 95% confidence intervals for all fluxes, are also provided in **Additional File 2.** The flux distributions of *P. putida* KT2440 and strain SCA3$_{PK\text{-}Tn}$/pS438•*pta*^{Ec} were visualized by mapping the computed flux values onto custom metabolic maps using the R package *fluctuator*. The gluconate and 2KG uptake rates were combined, since their relative contribution could not be determined based on the carbon transitions.

2.10. Metabolite analyses via HPLC

Sugars and organic acids were analyzed using a Dionex Ultimate 3000 HPLC with an Aminex™ HPX-87X Ion Exclusion (300 × 7.8 mm) column (BioRad, Hercules, CA) as well as RI-150 refractive index and UV (260, 277, 304 and 210 nm) detectors. For analysis, the column was maintained at 65 °C and a 5 mM H_2SO_4 solution was used as the mobile phase at a flow rate of 0.5 mL min^{-1}. HPLC data were processed using the Chromeleon 7.1.3 software (Thermo Fisher Scientific), and compound concentrations were calculated from peak areas using calibration curves with five different standard concentrations.

2.11. Determination of in vitro phosphoketolase activity

PKT activity was determined in cell lysates according to the hydroxamate method adapted from Lipmann and Tuttle (1945). This assay relies on the reaction of enzymatically-produced Ac–P with hydroxylamine to form hydroxamate and inorganic phosphate; hydroxamate is converted into a ferric hydroxamate complex *via* addition of $FeCl_3$. The complex exhibits an orange-brown to purplish-brown color, depending on the Ac–P concentration, and can be quantified spectrophotometrically by absorbance readings between 480 and 540 nm ($FeCl_3$ shows no absorption at these wavelengths). For these determinations, *P. putida* strains were cultured overnight in 50 mL of LB medium supplemented with 0.5 mM 3-*m*Bz to induce *xfpk* expression. All following steps were performed on ice and with pre-chilled solutions. Cells were collected by centrifugation at 5000×*g* for 10 min at 4 °C, washed twice with phosphate buffer (50 mM phosphate buffer, 0.5 g L^{-1} L-cysteine, and 1 mM $MgCl_2$; pH = 6.5), and suspended in 3 mL of the same buffer. The suspensions were split into 1-mL aliquots in 2-mL cryotubes, and 0.3 g of acid-washed glass beads were added. Cells were lysed using a bead-beater homogenizer (BioSpec Products, Bartlesville, USA) at 6000 rpm (two cycles, 20 s). Clear lysates were obtained by centrifugation at 17,000×*g* for 2 min at 4 °C. The protein concentrations were determined *via* the Bradford assay (He, 2011), and all lysates were adjusted to the lowest concentration measured by adding phosphate buffer. The enzyme assay was performed in 1.5-mL micro reaction tubes; 600 µL of lysate was added to 150 µL of halogen solution (6 mg mL^{-1} NaF and 10 mg mL^{-1} iodoacetic acid) and 150 µL of 80 mg mL^{-1} D-F6P. The reaction mixtures were incubated at 30 °C, and 75-µL samples were taken in 10-min intervals. Samples were distributed into the wells of a 96-well plate pre-filled with 75 µL of 2 M hydroxylamine (freshly adjusted to pH = 7 with 1 M HCl) and incubated for 10 min at room temperature. Subsequently, 50 µL of 150 mg mL^{-1} trichloroacetic acid, 50 µL of 4 M HCl, and 50 µL of 50 g L^{-1} $FeCl_3$ in 0.1 M HCl were added to the mixture. After the last sample was processed, the absorption at 505 nm was measured for all samples in a Synergy H1 plate reader. A calibration curve with Ac–P (lithium salt) was created by subjecting solutions of different concentrations to the same assay procedure.

2.12. Whole-genome sequencing

The sequencing of chromosomal (and plasmid) DNA to analyze the effects of evolution was performed by Novogene (Cambridge, UK). The DNA content of strains was purified using the PureLink™ Genomic DNA Mini Kit (Invitrogen, CA, USA). The raw data was processed in Geneious Prime (2021).1.1 (Biomatters Ltd.) by read pairing, trimming (BBDuk plugin with settings [Trim adapters], [Trim low quality], [Minimum Quality: 20], [Trim Adapters based on paired read overhangs with a minimum overlap of 20], [Discard Short Reads, with minimum length 20]), and mapping to the reference genome sequence (with [Mapper: Geneious], [Medium Sensitivity], [Find structural variants, short insertions, and deletions of any size], and [Minimum support for structural variant discovery: 10 reads]). Sequence polymorphisms were identified by using the build-in *Find Variations/SNPs* function with default settings. Single-nucleotide polymorphisms (SNPs) found in both pre-evolved and evolved clones were discarded.

2.13. Data and statistical analyses

All experiments were performed at least in three independent biological replicates unless otherwise stated, and the mean values ± standard deviation are presented. Statistical significances were determined by calculating *P*-values with the T.Test function of Microsoft Excel (2016). Maximum exponential growth rates (μ_{max}) were determined by Gaussian process regression using the Python-based tool deODorizer (Swain et al., 2016). Average specific growth rates over the exponential phase (µ) were determined by fitting *ln*-transformed OD_{600} data against time to simple linear regressions. Biomass yields ($Y_{X/S}$) on substrates were determined as the slope of linear regressions on biomass-against-substrate plots. Biomass-specific substrate consumption rates (q_S) were calculated by dividing µ by $Y_{X/S}$, and metabolite secretion rates (q_P) by multiplying q_S with $Y_{P/S}$ (obtained as the slope from metabolite-against-substrate plots). The biomass-specific CO_2 production rate q_{CO2} was calculated by multiplying the slopes of linear CO_2-against-CDW regressions with µ. All linear regressions, as well as data visualizations, were performed in OriginPro 2021 (OriginLab Corporation); figures and diagrams were created in OriginPro 2021 and Adobe Illustrator 2020. Geneious Prime 2021.1.1 (Biomatters Ltd.) served as a database for any kind of DNA sequences, to design plasmids and constructs, and to analyze Sanger and NGS sequencing results.

3. Results

3.1. Design of a synthetic C2-auxotroph strain informed by genome-scale metabolic modeling and in silico analysis of a phosphoketolase-based synthetic metabolism

To generate a C2 auxotroph platform strain for evolutionary engineering applications, we employed an *in silico*-informed approach to identify native pathways involved in AcCoA supply (39 reactions) and consumption (19 reactions; Fig. 1A). Next, we performed FBA using the genome-scale reconstruction *i*JN1463 of *P. putida* KT2440 (Nogales et al., 2020) with glucose as the sole carbon source (Fig. 1B, in green). The flux towards all of the intermediates that contribute to biomass formation (representing the first step of the corresponding catabolic pathways) was computed for each reaction identified *via* FBA (Table S2), and the reactions were ranked according to their absolute flux value. With these reactions 'knocked-out' in *i*JN1463 (i.e., an *in silico* C2 auxotroph), the two possible reactions of a bifunctional PKT enzyme acting as both F6P phosphoketolase (FPK) and Xu5P phosphoketolase (XPK) were introduced into the model (Fig. 1B, in red).

Based on the stoichiometry constraints in the metabolic network, the maximum growth rate achievable by *P. putida* endowed with an alternative, PKT-based synthetic metabolism for glucose (0.61 h^{-1}) was close to that of the wild-type model (0.62 h^{-1}). The ED pathway (flux through

Edd and Eda) was completely inactive; therefore, the PKT pathway constitutes a feasible alternative to the ED pathway in this obligate aerobic bacterium. Under these conditions, all flux is channeled into the PP pathway, with a 7-fold increased 6-phosphogluconate (6PG) dehydrogenase (Gnd) activity compared to that in the wild-type model. The flux through the ribulose-5-phosphate 3-epimerase (Rpe) reaction is also greatly enhanced to provide F6P or Xu5P needed as precursors for the PKT reactions.

The flux distribution shown in Fig. 1B represents only one possible FBA solution in which PKT acts exclusively on F6P. However, there is an infinite number of possible flux distributions where the total flux (5.46) is distributed between FPK and XPK, providing equal amounts of Ac–P and G3P. PP pathway metabolite levels are balanced in each solution by the transaldolase (TalA) and transketolase (Tkt) reactions. In both simulations, glucose was exclusively fed into central metabolism through the 6PG route, contrasting with experimentally-determined flux distributions, in which only 78% of the consumed glucose enters the cells in the form of gluconate, 10% as glucose, and 12% as 2KG (Nikel et al., 2015). The equilibrating effect of the PP pathway enzymes potentially allows for a balanced flux through the PKT pathway and downstream glycolysis. Hence, no significant increase in anaplerotic reactions is observed. To experimentally complement these *in silico* predictions, a synthetic C2 auxotroph of *P. putida* (termed SCA) was constructed as explained in the next section.

3.2. A synthetic auxotroph of P. putida requires acetate to support growth on hexoses

Informed by the *in silico* prediction with *i*JN1463, a whole family of SCA strains was created with an increasing number of deletions of genes involved in the potential formation of AcCoA (Table S1, Table S2). The auxotrophy was confirmed by testing growth in DBM medium with various carbon sources (Fig. 2A, Figure S1A-E). All strains deficient in PDHc (i.e., strains SCA1, SCA3, SCA9, SCA15, and SCA18) could not grow within 120 h after inoculation with glucose as the carbon source (Fig. 2A, only the first 24 h are shown). These strains could not grow on fructose and gluconate, either (data not shown). Thus, the deletion of *aceE* and *aceF* suffices to establish auxotrophy for C2 compounds on glycolytic substrates in wild-type *P. putida*. Cells that only had PDHc inactivated (strain SCA3) were not impaired in their ability to utilize acetate as the only carbon source (Figure S1A; Table S3). Furthermore, when PDHc was left intact, the 14 implemented gene deletions in strain $SCA14_{PD}$ did not affect phenotypes on glycolytic substrates (Fig. 2A) or citrate, a TCA cycle metabolite and a preferred carbon substrate of *P. putida* (Figure S1B). However, removing several genes involved in the assimilation of amino acids, among other targets, resulted in decreased biomass yields and more pronounced diauxic shifts when grown in a rich medium (Fig. 2B).

Glucose (C6) and acetate (C2) are co-consumed by *P. putida* KT2440 (Figure S2). Glucose is used as an energy source as long as acetate is assimilated; upon acetate depletion, the carbon skeleton of glucose is utilized for biomass formation. Thus, growth of SCA strains could be restored *via* co-feeding acetate and glucose. To gain insights into the requirements for acetate as co-substrate, strain SCA3 was cultured in DBM medium containing 30 mM glucose as well as varying concentrations of potassium acetate (KAc, Figure S1C). The maximum biomass concentration reached by the strains showed a linear dependency on acetate when supplied up to 1.8 g L^{-1} (30 mM, Fig. 2C). At higher cell densities, oxygen supply becomes a limiting factor in microtiter plates due to low transfer rates, leading to a disproportional rise in cell densities at increasing substrate concentrations. Importantly, the maximum specific growth rate (μ_{max}) of strain SCA3 was equal to that of wild-type *P. putida* on glucose and acetate (Table S3).

The cumulative effects of 12 additional deletions in strain SCA15 led to a reduction in μ_{max} of ca. one-half while lowering the acetate-specific biomass yield ($Y_{X/S}$) by about one-third (Figure S1D and S1E; Table S3). The reduced μ_{max} and $Y_{X/S}$ were likely the results of glyoxylate shunt inactivation *via* deletion of malate synthase (*glcB*), causing all carbon moieties introduced into the TCA cycle in the form of acetate-derived AcCoA to be oxidized to CO_2. Thus, essential TCA cycle intermediates need to be replenished from the glycolytic end-metabolites Pyr and phosphoenolpyruvate (PEP). The inactivation of the glyoxylate shunt also prevented the utilization of acetate as the only carbon source by *P. putida* SCA15 (Figure S1A). All SCA strains, including *P. putida* SCA15, were still able to grow on citrate as the sole source of carbon—albeit severely impaired (Figure S1B). To rule out any side-activity of citrate synthase in the reverse direction, *gltA* was deleted alongside genes involved in carbon catabolite repression. However, the resulting strain, *P. putida* SCA18, was still able to grow on citrate as the sole carbon source, with no apparent growth deficiencies as compared to strain SCA15. These results formed the basis for establishing a synthetic assimilation route for sugars as indicated below.

3.3. Quantitative proteome analysis exposes the dependency of synthetic C2 auxotrophs on acetate and highlights potential bottlenecks for a functional phosphoketolase pathway

To uncover the effects of removing intracellular AcCoA sources, the quantitative proteome of exponentially-growing strains SCA3 and KT2440 was assessed *via* mass spectrometry with cells grown in DBM medium supplemented with 30 mM glucose and 30 mM acetate. Thereby, 3051 proteins were uniquely identified, of which 381 proteins were removed due to missing values (i.e., below the detection limit). From the remaining 2670 proteins, a total of 110 proteins differed significantly [false discovery rate (FDR) of $\leq$0.05] with an absolute $\log_2$(fold change) $\geq$ 1 (Figure S3). Among these, 45 were identified to display metabolic functions (Table S4). Within central carbon metabolism, a down-regulation of gluconokinase (GnuK), glucose-6-phosphate (G6P) 1-dehydrogenase [ZwfA (Volke et al., 2021)], and 6-phosphogluconolactonase (Pgl) was observed together with an up-regulation of 2-ketogluconate-6-phosphate reductase (KguD, Figure S4). This pattern suggests a shift from the preferred glucose utilization route [i.e., glucose oxidation and gluconate uptake (Nikel et al., 2015)] towards further oxidation to 2 KG and utilization thereof. We had observed that engineered *P. putida* strains convert glucose into 2 KG at significant rates if growth is hampered by genetic modifications (Nitschel et al., 2020).

Strain SCA3 showed a diverging pattern in the content of enzymes involved in anaplerotic reactions connecting the downstream EMP route with the TCA cycle. Compared to the wild-type strain, the oxaloacetate-producing Pyr carboxykinase (PycA and PycB) was downregulated by 70%. On the other hand, oxaloacetate decarboxylase (OadC, *PP_1389*) was upregulated by a factor of 6.4. The two enzymes constituting the glyoxylate shunt, isocitrate lyase (AceA) and malate synthase (GlcB), were 3.5- and 2-fold, respectively, more abundant in SCA3. Furthermore, two enzymes associated with fatty acid degradation (and conversely, AcCoA formation), AcCoA acetyltransferase (YqeF, 3.5-fold) and β-ketoadipyl-CoA thiolase subunit β (FadA, 1.6-fold)] were elevated in the engineered strain. (3*R*)-3-Hydroxydecanoyl-ACP dehydratase (FabA), associated with fatty acid biosynthesis, was downregulated by a factor of 0.6. The results of pathway enrichment analysis with pathways listed in the KEGG database are shown in Figures S5 and S6. These observations suggest a substantial utilization of acetate as a carbon substrate for central metabolism as opposed to energy provision. The abundance of fatty acid metabolism enzymes reflects the recruitment of lipid pools to replenish AcCoA, whereas the activity of the glyoxylate shunt is essential for acetate utilization since it bypasses the two decarboxylation steps of the TCA cycle. The conserved carbon could be further fed into gluconeogenesis, as indicated by the high OadC abundance.

To identify potential bottlenecks towards a synthetic PKT metabolism, the relative protein abundances for strain KT2440 grown on

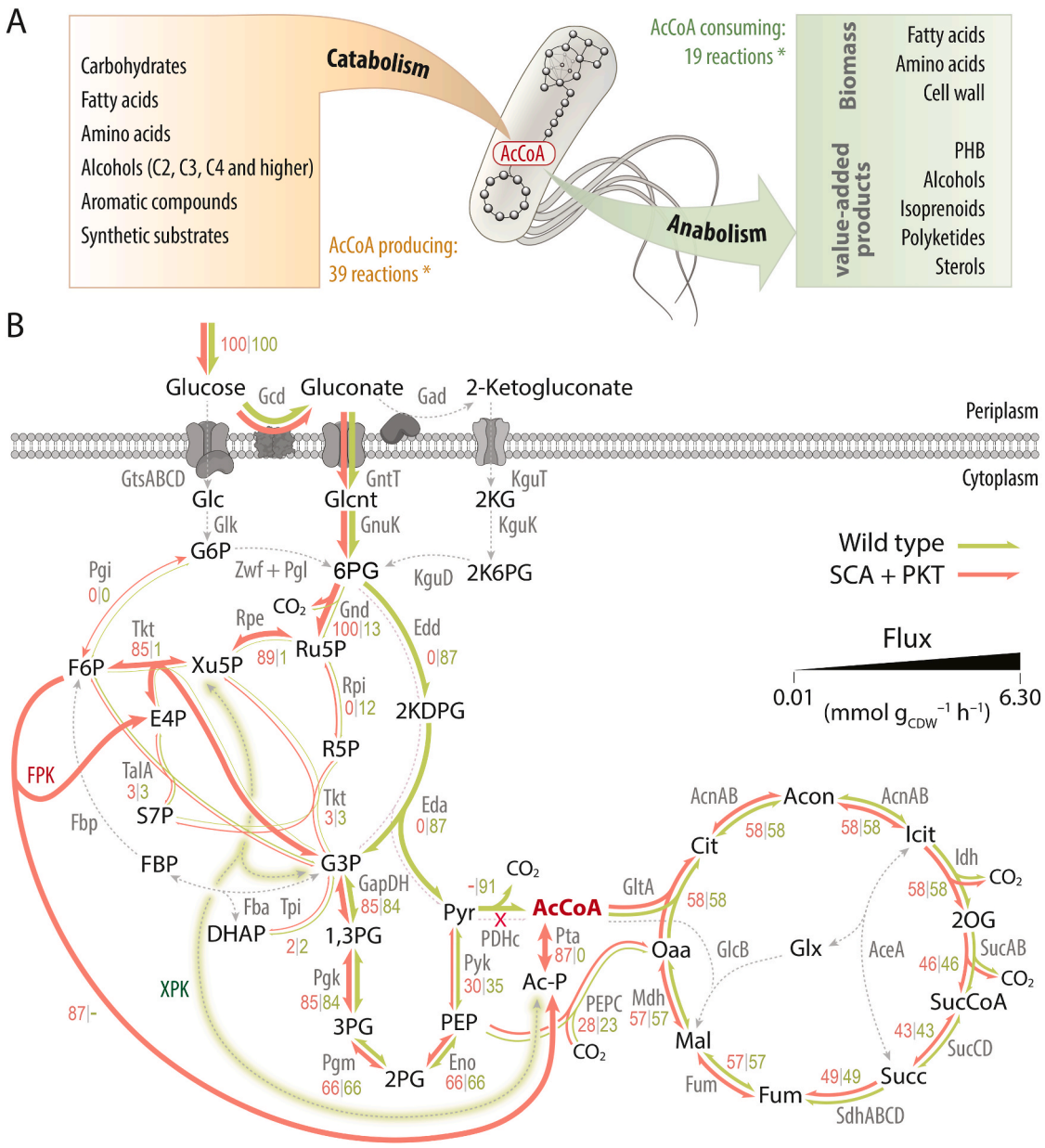

Fig. 1. Modeling the role of acetyl-coenzyme A in the central carbon metabolism of *P. putida* towards establishing a synthetic C2 metabolism. (A) Numerous carbon substrates are funneled through catabolic pathways with acetyl-coenzyme A (AcCoA) as the end- or side-product [the asterisk symbol (*) indicates the total number of reactions as listed in the BioCyc database (Karp et al., 2019)]. AcCoA serves as the starting point (or co-substrate) for the biosynthesis of multiple essential biomass constituents or secondary metabolites of industrial interest. *PHB*, poly(3-hydroxybutyrate). **(B)** *In silico* flux distributions estimated *via* the genome-scale reconstruction *i*JN1463 of *P. putida* KT2440. The flux distribution of the wild-type model with glucose as the sole carbon source is shown with green arrows; red arrows indicate fluxes after deleting AcCoA-producing pathways (SCA strains, Table 1) and introducing the two possible reactions catalyzed by PKT (which differ in the substrate used). The thicknesses of reaction arrows are drawn in scale reflecting their flux (from 0.01 to 6.30 mmol g_{CDW}^{-1} h^{-1}). Reactions with no detectable flux are drawn as dashed lines. Abbreviations for substrates and metabolites: 1,3PG, 1,3-bisphosphoglycerate; 2K6PG, 2-ketogluconate-6-P; 2PG, glycerate-2-P; 3PG, glycerate-3-P; 6PG, 6-phosphogluconate; 2KG, 2-ketogluconate; Ac–P, acetyl-P; CoA, coenzyme A; AcCoA, acetyl-CoA; DHAP, dihydroxyacetone-P; E4P, erythrose-4-P; F6P, fructose-6-P; FBP, fructose-1,6-bisphosphate; G3P, glyceraldehyde-3-P; G6P, glucose-6-P; Glc, glucose; Glcnt, gluconate; KDPG, 2-keto-3-deoxy-6-phosphogluconate; PEP, phosphoenolpyruvate; R5P, ribose-5-P; Ru5P, ribulose-5-P; S7P, sedoheptulose-7-P; 2OG, 2-oxoglutarate; Acon, aconitate; Cit, citrate; Fum, fumarate; Glx, glyoxylate; Icit, isocitrate; Mal, malate; Oaa, oxaloacetate; Pyr, pyruvate; Succ, succinate; SucCoA, succinyl-CoA; and Xu5P, xylulose-5-P. Abbreviations for enzymes: AceA, Icit lyase; AcnAB, aconitase; Edd, 6PG dehydratase; Eda, 2K6PG aldolase; Eno, enolase; Fba, FBP aldolase; FPK, F6P phosphoketolase; Fbp, fructose-1,6-bisphosphatase; Fum, fumarate hydratase; GADH, gluconate dehydrogenase; GapDH, G3P dehydrogenase; Gcd, glucose dehydrogenase; GlcB, Mal synthase; Glk, glucose kinase; GltA, Cit synthase; Gnd, 6PG dehydrogenase; GntT, gluconate/H^+ symporter; GnuK, gluconate kinase; GtsABCD, D-glucose ABC transporter; MaeB, malic enzyme; Idh, isocitrate dehydrogenase; KguD, 2K6PG reductase; KguK, 2KG kinase; KguT, putative 2KG transporter; Mdh, malate dehydrogenase; PEPC, PEP carboxylase; PC, Pyr carboxylase; PDHc, Pyr dehydrogenase complex; Pgi, phosphohexose isomerase; Pgk, phosphoglycerate kinase; Pgl, 6-phosphogluconolactonase; Pgm, phosphoglycerate mutase; Pta, phosphate acetyltransferase; Pyk, Pyr kinase; Rpe, Ru5P 3-epimerase; Rpi, R5P isomerase; Sdh, Succ dehydrogenase; SucAB, 2OG dehydrogenase; SucCD, succinyl-CoA synthetase; Tal, transaldolase; Tkt, transketolase; Tpi, triosephosphate isomerase; and Zwf, G6P 1-dehydrogenase. Only compounds participating in carbon transitions are shown, and reactions catalyzed by multiple isoenzymes (e.g., Pgi, Zwf, or GapDH), were lumped together for the sake of simplicity. The figures shown within the map show the relative fluxes normalized to the glucose uptake rate (6.30 mmol g_{CDW}^{-1} h^{-1}, set as 100).

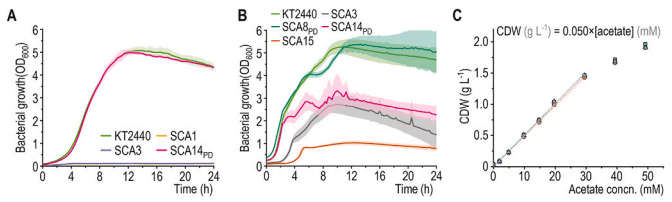

Fig. 2. Phenotypic characterization of synthetic C2 auxotrophs. Both the SCA strains and wild-type *P. putida* KT2440 were cultured in microtiter plates (96-well) in these experiments either in **(A)** DBM medium supplemented with 30 mM glucose as the sole source of carbon or **(B)** LB medium. In all cases, the error bars represent standard deviations from three independent biological replicates, indicated by shaded ribbons around the growth curves. **(C)** Growth-dependency of *P. putida* SCA3 on acetate as the only source of C2 units for biomass formation (concentration of cell dry weight, *CDW*). The strain was grown in DBM medium supplemented with 30 mM glucose and varying concentrations of acetate as indicated. Shown are the individual measurements and linear correlations of three independent biological replicates. *Concn.*, concentration.

glucose were compared to that during growth on glucose and acetate (Figure S7). Most enzymes within upstream glycolysis were produced at statistically significantly lower amounts in the presence of acetate as co-substrate. Only Pta was expressed 8-fold higher in the presence of glucose and acetate compared with sugar cultures. The functionality of Pta in the conversion of Ac–P to AcCoA was experimentally demonstrated (Nikel and de Lorenzo, 2013), but the low abundance in glucose-grown *P. putida* suggests a potential bottleneck towards a functional PKT pathway. Additionally, the low flux through the PP pathway in *P. putida* (Nikel et al., 2015) was reflected in the protein levels of PP pathway enzymes in all experimental conditions—except for Tkt and Tal. Flux control over these reactions is likely exerted on a metabolite level (Udaondo et al., 2018), allowing for a quicker response to changes in the flux distribution within the EDEMP cycle. Although it was not known how the proteome of an SCA strain behaves in the presence of glucose as sole carbon source, and the results presented in this section only indicate possible limitations in the host, these observations suggest that fluxes through the non-oxidative branch of the PP route and conversion of Ac–P to AcCoA should be enhanced to establish a synthetic PKT metabolism in *P. putida*.

3.4. Implementing the phosphoketolase pathway in a synthetic C2 auxotroph restores prototrophy on glucose

The PKT shunt was implemented by introducing the gene encoding Xfpk^{Ba} from *Bifidobacterium adolescentis* E194 in a landing pad in the intergenic region between *PP_0013* (*gyrB*) and *PP_5421* (Wirth et al., 2020) of the chromosome of *P. putida* SCA3, yielding strain SCA3$_{PK}$ (Table 1). Xfpk^{Ba} is a bifunctional PKT enzyme with a reported *in vitro* activity ratio on Xu5P:F6P of 3:2 (Bergman et al., 2016). Additionally, strain SCA3$_{PK}$ was transformed with plasmid pS438•*pta*^{Ec} (encoding the highly-active Pta enzyme from *E. coli*) to boost Ac–P conversion into AcCoA. In this plasmid, *pta*^{Ec} is placed under transcriptional control of the XylS/*Pm* expression system, and the construct also provides XylS *in trans* to initiate transcription from the *Pm* promoter that leads to the expression of *xfpk*^{Ba} from the chromosome.

The production and functionality of Xfpk^{Ba} were tested *in vitro* with cell lysates *via* indirect chemical detection through the ferric hydroxamate method (Fig. 3A). To this end, the soluble fraction of cell-free extracts obtained from strains SCA3/pS438•*pta*^{Ec} and SCA3$_{PK}$/pS438•*pta*^{Ec} were adjusted to a final total protein concentration of 6 mg mL^{-1}, and the F6P-dependent formation of Ac–P was monitored over time. After 1 h of incubation, PKT activity in the sample containing Xfpk^{Ba} was made evident by the development of a red pigment, whereas no such coloration was observed in the absence of Xfpk^{Ba} (Fig. 3B). Fig. 3C shows the time-resolved PKT activity of the two cell lysates. No Ac–P was observed for the strain without *xfpk*^{Ba} (*P. putida* SCA3/pS438•*pta*^{Ec}), while lysates of strain SCA3$_{PK}$/pS438•*pta*^{Ec} converted F6P into Ac–P at a rate of 0.049 mmol Ac–P min^{-1}, corresponding to a specific activity of 8.2 μmol mg$^{-1}_{protein}$ min^{-1}. The results of the hydroxamate assay indicated that Xfpk^{Ba} was produced in an active form in *P. putida*. Two other Xfpk variants, chromosomally-introduced in SCA3 as codon-optimized *xfpk* genes from *Pseudomonas fluorescens* F113 and *Bifidobacterium mongoliense* YIT 10443, were tested under the same conditions but did not mediate any significant formation of Ac–P in cell-free extracts of the corresponding strains (data not shown).

To test whether Xfpk^{Ba} could restore the growth of synthetic C2 auxotrophs, *P. putida* SCA3$_{PK}$/pS438•*pta*^{Ec} and SCA3/pS438•*pta*^{Ec} were cultured in DBM medium supplemented with 10 mM glucose as well as 0.5 mM 3-*m*Bz as the inducer of *xfpk*^{Ba} expression (Fig. 3D). Indeed, the expression of both *xfba*^{Ba} and *pta*^{Ec} enabled glucose-dependent growth of *P. putida* SCA3$_{PK}$/pS438•*pta*^{Ec}, with a $Y_{X/S}$ of 0.02 g$_{CDW}$ g$^{-1}_{glc}$ and a μ_{max} of 0.06 h^{-1}—whereas supplying the XylS activator from plasmid pSEVA438 alone did not. As expected, *pta*^{Ec} expression alone did not promote bacterial growth (data not shown), indicating that Xfpk^{Ba} is actively involved in sugar catabolism.

As indicated in the previous sections, the reactions performed by 6PG dehydrogenase (Gnd) and ribulose-5-phosphate 3-epimerase (Rpe) were

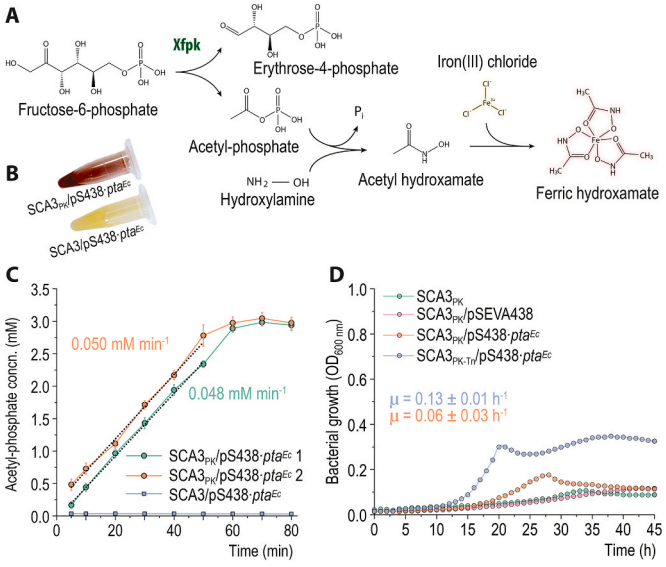

Fig. 3. Expression of *xfpk*^{Ba} in a synthetic C2 auxotroph of *P. putida*. Cell lysates were prepared from cultures grown in LB medium with 0.5 mM 3-methylbenzoate (3-*m*Bz). A total protein concentration of 6 mg mL^{-1} was used for the *in vitro* conversion of F6P to Ac–P, the concentration of which was determined using the ferric hydroxamate method. **(A)** Reaction scheme of the PKT assay and product detection *via* ferric hydroxamate. **(B)** Reaction samples illustrating the enzymatic conversion Ac–P to ferric hydroxamate after a 1-h incubation; the red color in the assay for strain SCA3$_{PK}$/pS438•*pta*^{Ec} indicates Ac–P formation. **(C)** *In vitro* determination of FPK activity in *P. putida* SCA3/pS438•*pta*^{Ec} and SCA3$_{PK}$/pS438•*pta*^{Ec}. Each strain was tested in two independent biological replicates with three technical replicates; only one of two (comparable) biological replicates is shown for *P. putida* SCA3/pS438•*pta*^{Ec}. Error bars represent standard deviations from the independent biological replicates. **(D)** *In vivo* demonstration of PKT activity *via* growth coupling. Strain SCA3, harboring a chromosomally-integrated *xfpk*^{Ba} gene, with either no plasmid, or transformed with the empty pSEVA438 vector or plasmid pS438•*pta*^{Ec}, was used in these experiments. The same strain, transformed with plasmid pS438•*pta*^{Ec} and chromosomally-overexpressed *gntZ* and *rpe*, was also included in the assay. Cells were cultured in a microtiter plates (96-well) in DBM medium supplemented with 10 mM glucose and 0.5 mM 3-*m*Bz. The increase in optical density measured at 600 nm (OD$_{600}$) for strain SCA3$_{PK}$ could be attributed to the formation of colored compounds produced from 3-*m*Bz *via* oxidation. *Concn.*, concentration.

elevated in the optimal flux prediction obtained with the *i*JN1463 reconstruction for a C2-auxotrophic design as compared to the wild-type model. Thus, the expression of *gntZ* and *rpe* was enhanced *via* the chromosomal integration of a Tn*7*-encoded, synthetic *gntZ-rpe* operon. The expression of *gntZ* was controlled by the strong, constitutive P_{14g} promoter (Zobel et al., 2015) and the bi-cistronic translational coupling sequence *BCD10* (Mutalik et al., 2013). In this design, *rpe* was translationally coupled to *gntZ*. Chromosomal integration was achieved by cloning the synthetic operon into a mini-Tn*7* transposon borne by plasmid pTn*7*•P_{14g}*(BCD10)→gntZ-rpe* (Table 2). Overexpression of *gntZ* and *rpe* led to a 2- and 1.7-fold increase in μ_{max} and $Y_{X/S}$, respectively, for the resulting strain $SCA3_{PK\text{-}Tn}$/pS438•pta^{Ec} compared to $SCA3_{PK}$/pS438•pta^{Ec} (Fig. 3D, Table 3). Hence, and as predicted by FBA simulations, the implementation of a PKT bypass, combined with increasing Gnd, Rpe, and Pta production, restored hexose-dependent growth of a C2-auxotroph strain. The growth rate and biomass yield for strain $SCA3_{PK}$/pS438•pta^{Ec} were deemed sufficient to support evolutionary engineering towards enhancing growth of engineered *P. putida* on sugars.

3.5. Adaptive laboratory evolution integrates the phosphoketolase bypass into the metabolic network of P. putida

To optimize the flux through the synthetic PKT metabolism, strains SCA3, SCA3/pS438•pta^{Ec}, $SCA3_{Tn}$/pS438•pta^{Ec}, and $SCA3_{PK\text{-}Tn}$/pS438•pta^{Ec}, were subjected to ALE. After an estimated 140 generations (ca. 2 months) in DBM medium containing glucose, no significant difference in growth was observed for *P. putida* SCA3, SCA3/pS438•pta^{Ec}, and $SCA3_{Tn}$/pS438•pta^{Ec} (results not shown). However, clones isolated from the evolved population of strain $SCA3_{PK\text{-}Tn}$/pS438•pta^{Ec}, had a significant improvement in growth parameters, and doubled both μ_{max} and $Y_{X/S}$ (Fig. 4A, Table 3, and Figure S8A and S8B). The enhanced growth on glucose detected for this evolved variant, termed evo$SCA3_{PK\text{-}Tn}$_A/pS438•pta^{Ec} (Table 1), was stable even after five sub-culturing steps in a rich medium (LB). Hence, evolution—rather than a mere adaptation—was responsible for the improved phenotype. Other isolated variants from the ALE population, evo$SCA3_{PK\text{-}Tn}$_B/pS438•pta^{Ec} (Table 1), did not show any improved phenotype compared to the *naïve* strain (Figure S9).

When grown on gluconate (i.e., a more oxidized sugar than glucose), the growth rate of the evolved clones was not significantly altered. However, *P. putida* evo$SCA3_{PK\text{-}Tn}$_A/pS438•pta^{Ec} reached only 36% of the cell density on glucose (Figure S8B). This $Y_{X/S}$ reduction suggests a stoichiometric bottleneck in the regeneration of either energy or reducing equivalents on gluconate. During growth on glucose, 26% of membrane-bound ubiquinol in the electron transport chain is predicted to be produced by direct glucose oxidation (suggested by FBA simulations with *i*JN1463), acting as an ATP source. Alternatively, *P. putida* can produce NAD(P)H *via* the oxidation of G6P, contributing to the intracellular pool of reducing equivalents (Volke et al., 2021). The basis for these features was investigated by quantitative proteomics of evo$SCA3_{PK\text{-}Tn}$_A/pS438•pta^{Ec} as disclosed in the next section. The cell density reached in cultures of the variant evo$SCA3_{PK\text{-}Tn}$_B/pS438•pta^{Ec}, in contrast, was deemed insufficient to allow further characterization with omic approaches (data not shown).

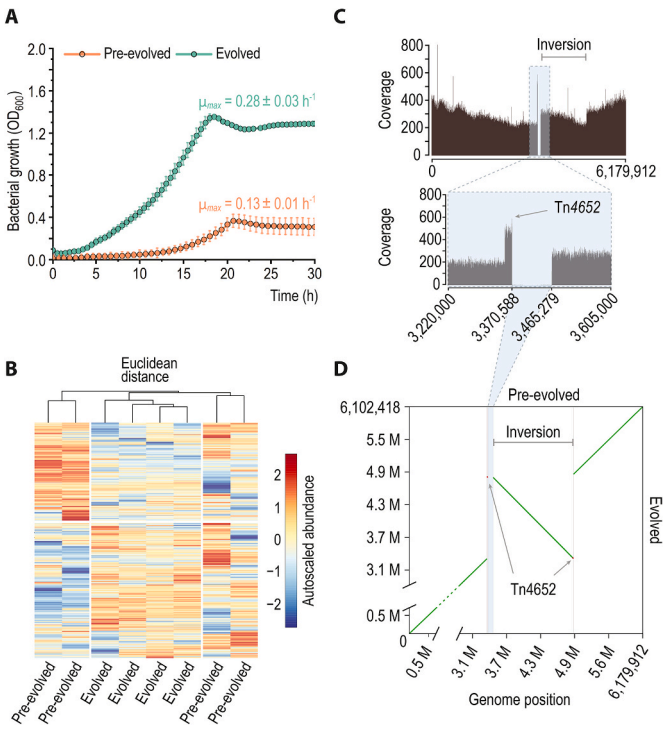

Fig. 4. Evolution of a synthetic PKT metabolism in engineered *P. putida*. **(A)** Batch (24-well plates) cultivation of the pre-evolved $SCA3_{PK\text{-}Tn}$/pS438•pta^{Ec} and evolved evo$SCA3_{PK\text{-}Tn}$_A/pS438•pta^{Ec} strains in DBM medium supplemented with 30 mM glucose and 0.5 mM 3-methylbenzoate (3-*m*Bz). OD_{600}, optical density measured at 600 nm. **(B)** Network-wide proteome of the evolved and pre-evolved *P. putida* strains ($SCA3_{PK\text{-}Tn}$/pS438•pta^{Ec} and evo$SCA3_{PK\text{-}Tn}$_A/pS438•pta^{Ec}, respectively). In this analysis, 3048 proteins were uniquely identified, of which 549 proteins were removed due to missing values. The protein abundance values were normalized, auto-scaled, and plotted according to their Euclidean distance for four independent biological replicates. **(C)** Coverage plot of whole-genome sequencing data (Illumina SBS technology) mapped to the reference chromosomal sequence of strain $SCA3_{PK\text{-}Tn}$. The progression of sequencing coverage downstream of the deletion indicates the inversion of a large chromosomal segment in strain evo$SCA3_{PK\text{-}Tn}$_A. **(D)** Dot plot of the reconstructed chromosomal sequence of *P. putida* evo$SCA3_{PK\text{-}Tn}$_A compared to the reference sequence in the pre-evolved strain $SCA3_{PK\text{-}Tn}$. A duplicated DNA segment comprising the Tn*4652* transposon is illustrated in red, the deleted stretch is shaded in blue.

3.6. Comparative proteomic profiling of pre-evolved and evolved P. putida carrying a synthetic phosphoketolase metabolism

Comparative proteome analysis of glucose-grown *P. putida* $SCA3_{PK\text{-}}$

Table 3
Quantitative physiology parameters of glucose-grown PKT-shunt *P. putida* strains.

P. putida strain	Modifications			Carbon source	μ_{max} (h^{-1})	Biomass yield, $Y_{X/S}$ (g_{CDW} g_S^{-1})
	xfpk^{Ba}	*gntZ-rpe*	Evolved			
SCA3	–	Native	–	Glucose	N.G.	N.G.
$SCA3_{PK}$/pS438•pta^{Ec} (pre-evolved/evolved)	+	Native	–/+	Glucose	0.06 ± 0.03	0.02 ± 0.01
$SCA3_{PK\text{-}Tn}$/pS438•pta^{Ec} (pre-evolved)	+	Overexpressed	–	Glucose	0.13 ± 0.01	0.04 ± 0.01
evo$SCA3_{PK\text{-}Tn}$_A/pS438•pta^{Ec} (evolved)	+	Overexpressed	+	Glucose	0.28 ± 0.03	0.09 ± 0.01
evo$SCA3_{PK\text{-}Tn}$_A/pS438•pta^{Ec} (evolved)	+	Overexpressed	+	Gluconate	0.23 ± 0.03	0.03 ± 0.01

Maximum exponential growth rates (μ_{max}) were determined *via* Gaussian process regression for growth experiments in microtiter plates. Biomass yields ($Y_{X/S}$), in g of cell dry weight (g_{CDW}) per g of substrate (g_S), were calculated for each indicated substrate. Given are the average values ± standard deviation from at least three independent biological replicates. *N.G.*, no growth.

$_{Tn}$/pS438•*pta*^{Ec} and its ALE-derivative evoSCA3$_{PK\text{-}Tn}$_A/pS438•*pta*^{Ec} revealed that only 24 proteins had significantly altered abundance (Figure S10; Table S5). However, pre-evolved clones exhibited noticeably higher variability in their protein content, reflected in large Euclidean distances between each clone's dataset (Fig. 4B). Most notably, ThiL, encoding thiamine monophosphate kinase, could not be detected in the proteome of *P. putida* SCA3$_{PK\text{-}Tn}$/pS438•*pta*^{Ec}, whereas it was present in evoSCA3$_{PK\text{-}Tn}$_A/pS438•*pta*^{Ec}. Overexpression of *thiL* could be the result of increased thiamine pyrophosphate demands due to the heterologous production of Xfpk^{Ba}. Secondly, the ethanolamine ammonia-lyase EutB was highly overrepresented in all evolved clones. The *eutB* gene had been added to the list of AcCoA-forming reactions (Table S2) due to its potential to form acetaldehyde (and consequently, AcCoA) from ethanolamine, the most abundant phospholipid head group in bacteria. Lastly, the abundance of GltD (glutamate synthase, subunit β) was increased by 3-fold. To investigate effects not captured by proteomic analysis and to elucidate genetic differences between the evoSCA3$_{PK\text{-}Tn}$_A/pS438•*pta*^{Ec} and evoSCA3$_{PK\text{-}Tn}$_B/pS438•*pta*^{Ec} clones, we adopted functional genomics to study potential modifications brought about by ALE.

3.7. Large-scale structural reorganizations occurred via transposition of mobile genetic elements

Two evolved *P. putida* clones with enhanced growth on glucose (i.e., evoSCA3$_{PK\text{-}Tn}$_A/pS438•*pta*^{Ec}), two evolved clones without growth improvement (i.e., evoSCA3$_{PK\text{-}Tn}$_B/pS438•*pta*^{Ec}), and four pre-evolved isolates were subjected to whole-genome sequencing. Polymorphisms that were identified in both pre-evolved and evolved clones were discarded. No mutations were found in plasmid pS438•*pta*^{Ec} and, based on the read coverage over the plasmid in relation to the average coverage over the chromosome sequence, its copy number seem to have remained unaltered. Only a single mutation could be identified in *P. putida* evoSCA3$_{PK\text{-}Tn}$_B, i.e., a point mutation in *tilS* (*PP_1608*, Table 1) that was also found in the chromosome of both evoSCA3$_{PK\text{-}Tn}$_A clones. In addition, a segment of 94,691 bp was absent in the read coverage of the otherwise isogenic evoSCA3$_{PK\text{-}Tn}$_A clones (Fig. 4C). This chromosomal region stretches from *PP_2985* to *PP_3089* (116 predicted genes), and harbors the previously identified 35.6-kb long prophage 2 [*PP_3026-PP_3066* (Martínez-García et al., 2014a; Wu et al., 2011)]. The excision of this prophage has not been reported so far in *P. putida* KT2440. Furthermore, the segment is located 1111 bp downstream of the Tn*4652* transposon, activated under carbon starvation and creating fusion promoters on both ends upon insertion into a target locus with low sequence specificity (Hõrak and Kivisaar, 1998; Ilves et al., 2001; Kivistik et al., 2007; Martínez-García et al., 2014b). In the course of evolution, Tn*4652* was duplicated and inserted into the gene encoding the flagellar biosynthesis protein FlhA. Removal of the flagellar machinery affects the energy status and reducing power availability of *P. putida* KT2440, resulting in multifaceted physiological improvements (Martínez-García et al., 2014c). Downstream of the insertion site, the flagellar operon continues with *PP_4345*, encoding a GntR family transcriptional regulator, and *ddlA*, encoding D-alanine−D-alanine ligase A. Accordingly, DdlA was found to be significantly overrepresented in the proteome of *P. putida* evoSCA3$_{PK\text{-}Tn}$_A (Figure S10), likely as result of enhanced transcriptional activity downstream of Tn*4652*. In conjunction with the 94,691-bp deletion, the 1,458,179-bp chromosomal segment flanked by both Tn*4652* copies was inverted (Fig. 4D)—which could have wide-ranging effects on the three-dimensional structure of the chromosome and therefore on gene regulation.

A full list of genes located within the deleted 94.7-kb region is given in Table S6. The absence of the 94.7-kb chromosomal sequence was confirmed *via* PCR-amplification of the locus (Figure S11). Apart from many proteins with unknown functions, an array of functions contributing to the production of pyocins are encoded within this region, as well as proteins with predicted regulatory and enzymatic roles. Potential regulatory proteins are FlaR (DNA topology modulation kinase), PP_3006 (ECF family RNA polymerase σ^{70} factor), PP_3002 (AraC family transcriptional regulator), ClpP (ATP-dependent protease), PP_5558 (Xre family transcriptional regulator), PP_3086 (RNA polymerase σ^{70} factor), PP_3075 (putative transcriptional regulator), and PP_3087 (excinuclease ABC subunit A). While the exact function of these proteins have not been characterized, the loss of *flaR*, *PP_3006*, *clpP*, *PP_3086*, and *PP_3086* could have caused systemic effects on DNA topology, DNA transcription, and/or protein degradation. Within the set of enzymes encoded in the missing chromosomal region, *PP_3071*, an acetoacetyl-CoA synthetase, could have a direct effect on the intracellular AcCoA concentration. Out of the 116 predicted genes within the deleted genome section, only 27 were uniquely identified within the proteome dataset discussed in the previous section. Most of these had a relatively low abundance within the dataset, also in pre-evolved strain SCA3$_{PK\text{-}Tn}$/pS438•*pta*^{Ec}. Out of this subset, six proteins were further removed from the analysis due to missing values (i.e., below the detection limit). Consequently, no definite conclusions can be drawn about the contribution of proteins encoded in the missing genomic region to the improved phenotype of evoSCA3$_{PK\text{-}Tn}$_A/pS438•*pta*^{Ec}. Regardless, the next step was to evaluate the performance of evolved clones of *P. putida*, bearing a synthetic PKT metabolism, under conditions compatible with sugar-dependent bioproduction.

3.8. The synthetic PKT metabolism enables conservation of carbon during growth on glucose

To characterize the physiology of evolved PKT-dependent *P. putida* evoSCA3$_{PK\text{-}Tn}$_A/pS438•*pta*^{Ec}, aerobic batch fermentations were performed in bioreactors under controlled conditions (using glucose as the only carbon substrate at 30 mM), and compared to wild-type strain KT2440 (Fig. 5A–D). Fig. 5A shows the time-resolved measurements for the dissolved oxygen concentration (DO), biomass, differential CO_2 formation rates, and extracellular metabolite concentrations (i.e., glucose, gluconate, 2KG, and Pyr).

Wild-type strain KT2440 reached its maximum cell density at an OD_{600} of 5.4 within 11 h ($\mu = 0.57\ h^{-1}$), while strain evoSCA3$_{PK\text{-}Tn}$_A/pS438•*pta*^{Ec} grew with a $\mu = 0.19\ h^{-1}$ to a maximum OD_{600} of 1.5 within 18 h. Accompanied by transient secretion of gluconate ($\leq$2.4 mM) and 2KG ($\leq$3.2 mM), the wild-type *P. putida* strain consumed the substrate (all three forms of the sugar) at $q_S = 8.12$ mmol $g_{CDW}^{-1}\ h^{-1}$ over the exponential growth phase (Fig. 5D), and the $Y_{X/S}$ on glucose was 0.40 $g_{CDW}\ g_{Glc}^{-1}$. No metabolites other than the three six-carbon moieties were detected in the medium. The growth profile of strain evoSCA3$_{PK\text{-}Tn}$_A/pS438•*pta*^{Ec} resembled that previously observed during physiological characterizations in 24-well plates (Fig. 4A, Figure S8). Glucose and its two oxidized products were consumed with a combined $q_S = 2.91$ mmol $g_{CDW}^{-1}\ h^{-1}$, and biomass was formed with $Y_{X/S}$ of 0.47 $g_{CDW}\ g_{C6}^{-1}$ and 0.09 $g_{CDW}\ g_{Glc}^{-1}$. Besides, evoSCA3$_{PK\text{-}Tn}$_A/pS438•*pta*^{Ec} secreted significant amounts of Pyr (which accumulated in the medium up to 14.6 mM) with a specific rate of 4.79 $mmol_{Pyr}\ g_{CDW}^{-1}\ h^{-1}$. Pyr production occurred in parallel to glucose consumption, and no re-consumption occurred after the cells reached the stationary phase. The accumulation of Pyr indicates a strong activity of the ED pathway, involving the splitting of 2KDPG into Pyr and G3P.

The synthetic PKT metabolism reduced the amount of CO_2 produced per C-mol of biomass by 46% compared to the wild-type strain (Fig. 5B). Two-thirds of the glucose supplied was oxidized to 2KG, secreted into the medium at a specific rate of 8.64 $mmol_{2KG}\ g_{CDW}^{-1}\ h^{-1}$. With a significant fraction of glucose being exclusively used as an energy source, the biomass yield from the consumed carbon was higher in evoSCA3$_{PK\text{-}Tn}$_A/pS438•*pta*^{Ec} compared to wild-type strain KT2440. Fig. 5C shows the carbon balance at the end of the growth phase for strain KT2440 (11 h) and evoSCA3$_{PK\text{-}Tn}$_A/pS438•*pta*^{Ec} (18 h), including all measured carbon-containing entities. A small residual amount of carbon could not be attributed to any of the detected metabolites for strain KT2440, likely

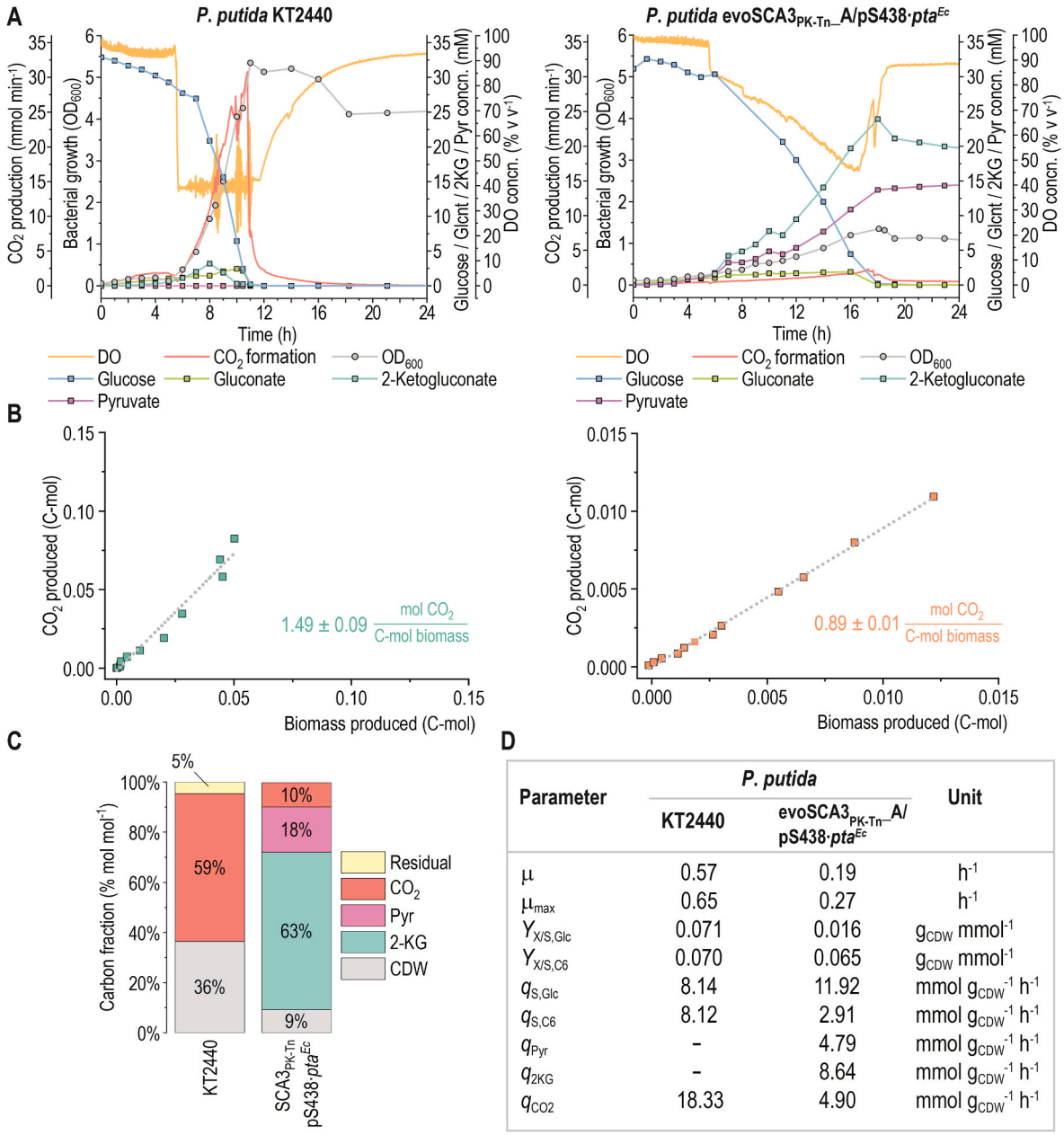

D

Parameter	*P. putida* KT2440	*P. putida* evoSCA3$_{PK\text{-}Tn}$_A/pS438·*pta*^{Ec}	Unit
μ	0.57	0.19	h^{-1}
μ_{max}	0.65	0.27	h^{-1}
$Y_{X/S,Glc}$	0.071	0.016	g_{CDW} $mmol^{-1}$
$Y_{X/S,C6}$	0.070	0.065	g_{CDW} $mmol^{-1}$
$q_{S,Glc}$	8.14	11.92	mmol g_{CDW}^{-1} h^{-1}
$q_{S,C6}$	8.12	2.91	mmol g_{CDW}^{-1} h^{-1}
q_{Pyr}	–	4.79	mmol g_{CDW}^{-1} h^{-1}
q_{2KG}	–	8.64	mmol g_{CDW}^{-1} h^{-1}
q_{CO2}	18.33	4.90	mmol g_{CDW}^{-1} h^{-1}

Fig. 5. Bioreactor cultivation of *P. putida* KT2440 and the evolved strain evoSCA3$_{PK\text{-}Tn}$_A/pS438•*pta*^{Ec}. Cells were grown in lab-scale bioreactors in batch mode in DBM medium supplemented with 30 mM glucose and, for evoSCA3$_{PK\text{-}Tn}$_A/pS438•*pta*^{Ec}, 0.5 mM 3-methylbenzoate (3-*m*Bz). (A) Selected process parameters and concentration of substrates, metabolites, and biomass over time. No pyruvate could be detected in the medium of wild-type strain KT2440. OD_{600}, optical density measured at 600 nm. (B) Correlation of the cumulative CO_2 produced (C-mol) with biomass (C-mol) at different sampling time points. (C) Carbon balance for batch fermentations. Shown are all carbon-containing entities measured at the end of the growth phases for each strain; carbon fractions represent the relative value of each chemical species compared to the overall amount of C-mol at the beginning of the fermentations. The amount of CO_2 was determined *via* the integration of measured CO_2 production rates over the whole fermentation time. (D) Summary of physiological parameters determined for bioreactor cultivations over the exponential growth phase (2–14 h). *Concn.*, concentration.

due to inaccuracies in the measurement of biomass concentrations or the volume left in the bioreactor. Both strains had fully consumed all supplied glucose by the end of the growth phase. The only carbon species identified for KT2440 were biomass (ca. 33% of the total carbon balance) and CO_2 (the remaining 64%). On the other hand, strain evoSCA3$_{PK\text{-}Tn}$_A/pS438•*pta*^{Ec} converted 81% of the supplied carbon into 2KG and Pyr. The cause of this drastic overflow metabolism was explored in detail by unraveling the distribution of intracellular metabolic fluxes as explained below.

3.9. ^{13}C-based metabolic flux analysis reveals a hybrid Entner-Doudoroff–phosphoketolase metabolism

The co-utilization of the ED pathway and the synthetic PKT shunt resulted in the pronounced overflow of 2KG and Pyr, suggesting an imbalance in the dissimilation of glucose towards biomass formation. To thoroughly characterize this metabolic architecture, we performed labeling experiments with [3–$^{13}C_1$]-glucose, [4–$^{13}C_1$]-glucose, or a mixture of each 50% unlabelled and uniformly labeled glucose ([U–$^{13}C_6$]-glucose, Fig. 6). The high conservation of glucose ^{13}C-3 and ^{13}C-4 units in the metabolites of interest allowed for the precise

resolution of every flux node, including reactions to and contributions of the two Xfpk^{Ba} activities, acting on either F6P or Xu5P. The use of 50% [U–$^{13}C_6$]-glucose, in contrast, helped to further increase the accuracy in the determination of flux ratios in the PP pathway as well as the cycling within the EDEMP architecture. Strain evoSCA3$_{PK\text{-}Tn}$_A/pS438•*pta*^{Ec} produced CO_2 at a rate that amounts to 20% of wild-type *P. putida* KT2440 (Figure S12), as determined for the bioreactor fermentations—underscoring the significant re-routing of carbon towards metabolite and biomass formation rather than oxidative decarboxylation. The PDHc reaction was entirely inactive in the network, as expected upon deleting *aceEF*.

Consistent with initial predictions *via* FBA, high activities within the PP pathway support the utilization of the Xfpk^{Ba}-based network architecture. Overexpression of *gntZ* and *rpe* resulted in an equal partitioning between the ED pathway and the oxidative PP route, and almost all of the Ru5P generated was converted to Xu5P. One-third thereof was cleaved by Xfpk^{Ba} into G3P and Ac–P. The remaining two-thirds were used by Tkt to recycle the E4P formed *via* the FPK activity of Xfpk^{Ba} back to F6P. This situation resulted in a significant flux towards G3P through the PP pathway, of which a major fraction (65%) was recycled through the EDEMP cycle to produce reducing equivalents *via* G6P oxidation (and 6PG decarboxylation). G3P formed through the ED pathway was further processed in the downstream glycolysis to PEP and Pyr. Around 70% of the ED-derived Pyr was secreted into the medium, while the remainder was either deployed in biomass-forming pathways or funneled into the TCA cycle through CO_2-incorporating anaplerotic reactions. Half of the AcCoA formed through the FPK and XPK reactions was used for biomass constituents; the rest fueled the TCA cycle. In there, AcCoA was partially utilized to produce the essential biomass precursor 2OG (concomitant with the formation of NADH and CO_2). The remaining carbon within AcCoA was preserved by the glyoxylate shunt.

The energy metabolism of wild-type *P. putida* KT2440 and strain evoSCA3$_{PK\text{-}Tn}$_A/pS438•*pta*^{Ec} significantly differed. In the wild-type strain, approximately 60% of the reducing equivalents used for ATP generation *via* oxidative phosphorylation were formed in the TCA cycle in the form of NADH and $FADH_2$ (Figure S12; Table S7). The remaining energy-generating reducing equivalents were produced *via* G3P oxidation (14%) as well as periplasmic glucose oxidation (22%). In *P. putida* evoSCA3$_{PK\text{-}Tn}$_A/pS438•*pta*^{Ec}, this balance was quite different. Less than 1% of the electrons for the respiratory chain were generated in reactions of the TCA cycle, whereas the two periplasmic glucose oxidation steps provided the largest share to the NADH, $FADH_2$, and UQH_2 pools. The remainder was provided by the oxidation of G3P.

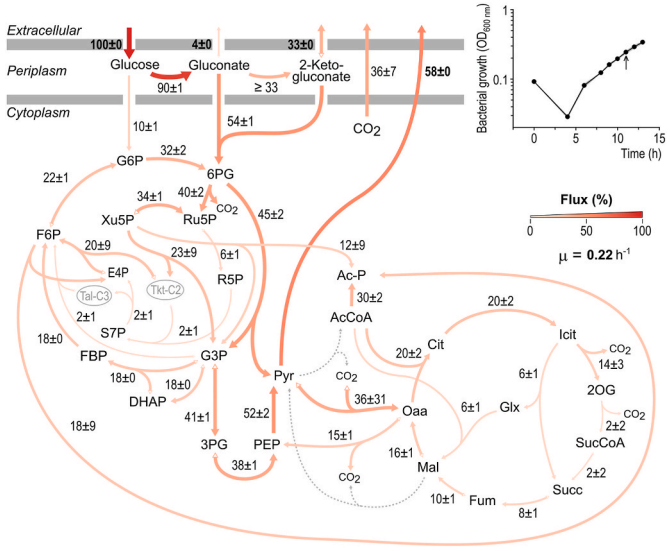

Fig. 6. *In vivo* distribution of carbon fluxes in the evolved *P. putida* evoSCA3$_{PK\text{-}Tn}$_A/pS438•*pta*^{Ec} strain grown on glucose as the only carbon source. Experimentally-determined rates were set as fixed parameters as follows: glucose consumption rate, 14.08 ± 1.15 mmol g_{CDW}^{-1} h^{-1}; gluconate secretion rate, 0.52 ± 0.07 mmol g_{CDW}^{-1} h^{-1}; 2KG secretion rate, 4.65 ± 0.22 mmol g_{CDW}^{-1} h^{-1}; pyruvate secretion rate, 8.19 ± 0.18 mmol g_{CDW}^{-1} h^{-1}; and exponential growth rate, 0.22 ± 0.01 h^{-1}. All fluxes were normalized to the specific glucose consumption rate. Flux values represent the mean ± standard deviations from three independent biological replicates. Abbreviations are as explained in the legend to Fig. 1. The inset graph shows the average growth curve of all three replicates with standard deviations indicated as shaded ribbons. The sampling time point (at 11 h) is indicated by a black arrow.

4. Discussion and conclusions

4.1. A synthetic C2 auxotroph P. putida provides a tight selection regime for AcCoA-producing pathways and reveals unknown metabolic connectivities on gluconeogenic substrates

In this study, a genome-scale model-guided approach informed the design of synthetic C2-auxotroph selection platforms based on *P. putida* KT2440. The auxotrophy of the selection strains was experimentally confirmed and shown to be reversible upon acetate feeding. Thus, the SCA strains can be easily propagated by supplying acetate or by cultivation in complex media. The strong dependency of biomass formation on acetate provides a tight selection scheme with a large evolutionary landscape in which gradual improvements in the AcCoA supply stimulate fitness gains. In this sense, the deletion of *aceEF* proved to be sufficient to disrupt growth on glycolytic substrates. For strain SCA3, where deletion of *aceEF* was combined with Δ*bkdAA* and Δ*ltaE*, no effect of evolution on restoring prototrophy on glucose was observed. However, one AcCoA-forming enzyme targeted in our *in silico* strain design, EutB, was overrepresented in evolved strain evoSCA3$_{PK\text{-}Tn}$_A/pS438•*pta*^{Ec}. Phosphatidylethanolamine, the most abundant phospholipid in bacteria, is synthesized exclusively by phosphatidylserine decarboxylase (Cho et al., 2021; Schuiki and Daum, 2009). Thus, phosphatidylethanolamine biosynthesis and its degradation to acetaldehyde could be an alternative AcCoA source.

The additional deletions identified might be a prerequisite for the selection strategy to work on carbon substrates other than (acidic) sugars, as illustrated by the ability of all SCA strains to use citrate. In strain SCA15, all genes identified as sources of AcCoA, Ac–P, acetate, or acetaldehyde were deleted, and the *in silico* reconstruction was unable to form biomass in all FBA simulations. However, the strain still grew on citrate. Consequently, the additional deletion of *glcB*, *gltA*, and *prpC* was performed to rule out the reversibility of the three cognate reactions, i.e., malate synthase (McVey et al., 2017), citrate synthase (Klinke et al., 2000; Sievers et al., 1997), and 2-methylcitrate synthase (Brock et al., 2000; Maerker et al., 2005). Elimination of GlcB, GltA, and PrpC, however, did not affect growth of strain SCA18 on citrate. Hence, unknown enzymatic functions in *P. putida* seem to have established a biochemical route from citrate to AcCoA—highlighting the role of 'underground' metabolic functions that come into play in the absence of the main reactions that supply biomass precursors or redox equivalents (Volke et al., 2020a,b, 2022).

4.2. Evolutionary adaptation to the presence of the phosphoketolase bypass resulted in a network-wide genome and proteome restructuring

The FBA predictions guided our strategy to implement an alternative PKT-based glycolysis in a synthetic C2-auxotroph strain. Chromosomal integration of *B. adolescentis xfpk* and plasmid-based expression of *E. coli pta* provided sufficient flux through the PKT bypass to establish growth on glucose. In response to the low abundances of GntZ and Rpe observed in whole-proteome analyses, the production of both enzymes was artificially increased, further enhancing the growth on glucose. Adaptive evolution enabled strain evoSCA3$_{PK\text{-}Tn}$_A/pS438•*pta*^{Ec} to make another leap toward restoring growth on glucose, providing evidence for the

suitability of the implemented, artificial C2-sink as a selection pressure for ALE. To identify mechanisms responsible for the improved growth rate and biomass yield, we analyzed changes in the proteome that occurred during evolution. Remarkably, and in contrast to the local mutations normally observed in ALE programs, the effects of evolution may have stabilized a beneficial proteomic profile—rather than causing a gain of function by up- or down-regulating specific proteins. This notion is supported by the change in gene copy numbers caused by the inversion of a large chromosomal segment in actively-dividing polyploid bacteria (Pecoraro et al., 2011).

4.3. A flux split between the native ED and the synthetic phosphoketolase bypass creates a metabolic imbalance in synthetic C2 auxotrophs

During batch fermentation on glucose, the evolved, PKT-dependent strain evoSCA3$_{PK\text{-}Tn}$A/pS438•*pta*^{Ec} secreted significant amounts of Pyr and 2KG. Pyr accumulation as an overflow metabolite can be attributed to the removal of PDHc, and alternative entry reactions into the TCA cycle or backflow of Pyr through gluconeogenesis would require additional ATP. Disproportionate production of 2KG, in contrast, can occur in *P. putida* in two main scenarios: (i) genetic manipulations that impose bottlenecks in the supply of biomass constituents, or (ii) disrupting the intracellular redox balance [by decreasing the *supply* of NAD(P)H or increasing NADPH *demands via*, e.g., high levels of oxidative stress]. In the first case, periplasmic dehydrogenases convert glucose into its acid forms faster than they can be utilized for biomass formation. This behavior resembles the phenomenon of acetate overflow production in glucose-grown *E. coli* (Valgepea et al., 2010). In the second scenario, shortages within the pool of soluble electron carriers that feed anabolic reactions and fuel the electron transport chain for energy production could limit bacterial growth. To maintain a high and homeostatic energy charge ([ATP] + 0.5 [ADP])/([ATP] + [ADP] + [AMP]), required to drive biosynthetic reactions (Andersen and von Meyenburg, 1977; Atkinson, 1968; Ebert et al., 2011), glucose can be utilized as an energy source without dissimilation. The electrons removed from glucose or gluconate during periplasmic oxidation are transferred to the ubiquinone pool in the cytoplasmic membrane or $FADH_2$, respectively (An and Moe, 2016; Matsushita et al., 1979). Consequently, they no longer contribute to replenishing the intracellular pool of NAD(P)H. Transport of 2KG across the cytoplasmic membrane has not been thoroughly studied in *P. putida*. The uptake is assumed to be mediated by the major facilitator superfamily (MFS) transporter KguT (Daddaoua et al., 2010), and it occurs against a concentration gradient (Torrontegui et al., 1976)—likely enabled *via* H^+ symport. The utilization of 2KG requires the NADPH-dependent reduction of 2K6PG to 6PG (Nikel et al., 2015). The rate at which the two periplasmic glucose oxidation steps occur in *P. putida* has been shown to depend on oxygen availability (Pedersen et al., 2021). With a significantly higher oxygen transfer rate in a bioreactor setup compared to shaken-flask cultivations, strain evoSCA3$_{PK\text{-}Tn}$A/pS438•*pta*^{Ec} had a considerably higher q_{2KG} and thus a significant glucose depletion in bioreactors when compared to the ^{13}C tracer experiments. In shaken-flask cultures, a greater fraction of glucose and gluconate were imported into the cytoplasm. To compensate for the decreased transfer of electrons to the respiratory chain *via* gluconate oxidation, highly active ED-pathway reactions need to provide sufficient flux to G3P towards producing NADH (see below). This situation created a shift from 2KG as the primary overflow metabolite to Pyr. An increased dissimilation of the carbon substrate within intracellular central metabolism could also explain the elevated q_{CO2} observed in fluxomic experiment compared to bioreactor fermentations.

In wild-type *P. putida* KT2440 growing on glucose, NADH was produced predominantly by PDHc, 2OG dehydrogenase (SucAB), and malate dehydrogenase (MDH). The reactions producing NADPH are, in order of their relative contribution, isocitrate dehydrogenase (Icd), G6P 1-dehydrogenase (Zwf), 6PG dehydrogenase (Gnd), and malic enzyme (MaeB). High flux through the reaction catalyzed by G3P dehydrogenase (GapDH) may have a variable contribution to the NADH/NADPH pool owing to the simultaneous presence of isoforms with divergent substrate specificities. After inactivation of PDHc in strain evoSCA3$_{PK\text{-}Tn}$A/pS438•*pta*^{Ec}, the predominant source of NADH is GapDH. NADPH is produced by Gnd and Zwf, and, to a lesser extent, by MaeB and Icd. If glucose is oxidized to 2KG in the periplasm, 1 molecule of NADPH is required to reduce 2K6PG to 6PG before entering the ED pathway. Thus, the net yield of intracellular reducing equivalents obtained sums up to zero. If 6PG is fed into the PP pathway to supply substrates for Xfpk^{Ba}, the NADPH produced by Gnd can also only compensate for initial consumption. In order to produce more soluble electron carriers, a significant flux must be delivered into the TCA cycle, requiring either a higher flux fraction through the two PKT reactions or an increased contribution of anaplerotic reactions. Thereby, increased production of NAD(P)H would allow the use of 2KG, which further increases the biomass yield on glucose.

4.4. A synthetic, hybrid PKT-ED metabolism can be exploited for the efficient production of chemicals

The main goal of this study was to establish synthetic C2-auxotrophy as a selection scheme for synthetic metabolism through evolutionary engineering. While a significant growth optimization could be achieved during ALE, biomass formation was limited by insufficient production of energy-generating reducing equivalents. While 2KG overflow production needs to be addressed to increase the flux of carbon into the cytoplasm, the simultaneous activities of Edd/Eda and Xfpk^{Ba} provide ample substrate amounts for bioproduction from Pyr as the precursor [e.g., isobutanol (Nitschel et al., 2020), D-lactic acid (Akita et al., 2017; Ishida et al., 2006), or 2,3-butanediol (Song et al., 2019)]. With these prospects, this study provides not only an example of the usefulness of carefully-designed selection strains for evolutionary engineering but also reveals unconventional metabolic engineering strategies for microbial production.

CRediT authorship contribution statement

Nicolas T. Wirth: Conceptualization, Data curation, Formal analysis, Investigation, Methodology, Project administration, Software, Validation, Visualization, Writing – original draft, Writing – review & editing. **Nicolás Gurdo:** Investigation, Methodology, Validation. **Nicolas Krink:** Investigation, Methodology, Validation. **Àngela Vidal-Verdú:** Investigation. **Stefano Donati:** Investigation, Methodology, Formal analysis. **Lorena Férnandez-Cabezón:** Conceptualization. **Tune Wulff:** Investigation, Formal analysis. **Pablo I. Nikel:** Conceptualization, Project administration, Funding acquisition, Supervision, Resources, Writing – review & editing.

Declaration of competing interest

The authors declare that there are no competing interests associated with the contents of this article.

Data availability

Data will be made available on request.

Acknowledgments

The authors thank Marcus Medom Ryding for his help with functional genome analysis. L.F.C. was supported by the European Union's Horizon 2020 Research and Innovation Programme under the Marie Skłodowska-Curie grant agreement No. 839839 (*DONNA*). The financial support from The Novo Nordisk Foundation through grants NNF20CC0035580, *LiFe* (NNF18OC0034818) and *TARGET* (NNF21OC0067996), the Danish Council for Independent Research

(*SWEET*, DFF-Research Project 8021-00039B), and the European Union's Horizon 2020 Research and Innovation Programme under grant agreement No. 814418 (*SinFonia*) to P.I.N. is likewise gratefully acknowledged.

Appendix A. Supplementary data

Supplementary data to this article can be found online at https://doi.org/10.1016/j.ymben.2022.09.004.

References

Akita, H., Nakashima, N., Hoshino, T., 2017. Production of D-lactate using a pyruvate-producing *Escherichia coli* strain. Biosci. Biotechnol. Biochem. 81, 1452–1455.

An, R., Moe, L.A., 2016. Regulation of pyrroloquinoline quinone-dependent glucose dehydrogenase activity in the model rhizosphere-dwelling bacterium *Pseudomonas putida* KT2440. Appl. Environ. Microbiol. 82, 4955–4964.

Andersen, K.B., von Meyenburg, K., 1977. Charges of nicotinamide adenine nucleotides and adenylate energy charge as regulatory parameters of the metabolism in *Escherichia coli*. J. Biol. Chem. 252, 4151–4156.

Antoniewicz, M.R., Kelleher, J.K., Stephanopoulos, G., 2006. Determination of confidence intervals of metabolic fluxes estimated from stable isotope measurements. Metab. Eng. 8, 324–337.

Arias-Barrau, E., Olivera, E.R., Luengo, J.M., Fernández, C., Galán, B., García, J.L., Díaz, E., Miñambres, B., 2004. The homogentisate pathway: a central catabolic pathway involved in the degradation of L-phenylalanine, L-tyrosine, and 3-hydroxyphenylacetate in *Pseudomonas putida*. J. Bacteriol. 186, 5062–5077.

Atkinson, D.E., 1968. The energy charge of the adenylate pool as a regulatory parameter. Interaction with feedback modifiers. Biochemistry 7, 4030–4034.

Bagdasarian, M., Lurz, R., Rückert, B., Franklin, F.C.H., Bagdasarian, M.M., Frey, J., Timmis, K.N., 1981. Specific purpose plasmid cloning vectors. II. Broad host range, high copy number, RSF1010-derived vectors, and a host-vector system for gene cloning in *Pseudomonas*. Gene 16, 237–247.

Bar-Even, A., Flamholz, A., Noor, E., Milo, R., 2012. Rethinking glycolysis: on the biochemical logic of metabolic pathways. Nat. Chem. Biol. 8, 509–517.

Belda, E., van Heck, R.G.A., López-Sánchez, M.J., Cruveiller, S., Barbe, V., Fraser, C., Klenk, H.P., Petersen, J., Morgat, A., Nikel, P.I., Vallenet, D., Rouy, Z., Sekowska, A., Martins dos Santos, V.A.P., de Lorenzo, V., Danchin, A., Médigue, C., 2016. The revisited genome of *Pseudomonas putida* KT2440 enlightens its value as a robust metabolic *chassis*. Environ. Microbiol. 18, 3403–3424.

Bergman, A., Siewers, V., Nielsen, J., Chen, Y., 2016. Functional expression and evaluation of heterologous phosphoketolases in *Saccharomyces cerevisiae*. AMB Express 6, 115.

Bogorad, I.W., Lin, T.S., Liao, J.C., 2013. Synthetic non-oxidative glycolysis enables complete carbon conservation. Nature 502, 693–697.

Brock, M., Fischer, R., Linder, D., Buckel, W., 2000. Methylcitrate synthase from *Aspergillus nidulans*: implications for propionate as an antifungal agent. Mol. Microbiol. 35, 961–973.

Calero, P., Volke, D.C., Lowe, P.T., Gotfredsen, C.H., O'Hagan, D., Nikel, P.I., 2020. A fluoride-responsive genetic circuit enables *in vivo* biofluorination in engineered *Pseudomonas putida*. Nat. Commun. 11, 5045.

Cavaleiro, A.M., Kim, S.H., Seppälä, S., Nielsen, M.T., Nørholm, M.H., 2015. Accurate DNA assembly and genome engineering with optimized uracil excision cloning. ACS Synth. Biol. 4, 1042–1046.

Chang, D.E., Shin, S., Rhee, J.S., Pan, J.G., 1999. Acetate metabolism in a *pta* mutant of *Escherichia coli* W3110: importance of maintaining acetyl coenzyme A flux for growth and survival. J. Bacteriol. 181, 6656–6663.

Chavarría, M., Nikel, P.I., Pérez-Pantoja, D., de Lorenzo, V., 2013. The Entner-Doudoroff pathway empowers *Pseudomonas putida* KT2440 with a high tolerance to oxidative stress. Environ. Microbiol. 15, 1772–1785.

Cho, G., Lee, E., Kim, J., 2021. Structural insights into phosphatidylethanolamine formation in bacterial membrane biogenesis. Sci. Rep. 11, 5785.

Chohnan, S., Furukawa, H., Fujio, T., Nishihara, H., Takamura, Y., 1997. Changes in the size and composition of intracellular pools of nonesterified coenzyme A and coenzyme A thioesters in aerobic and facultatively anaerobic bacteria. Appl. Environ. Microbiol. 63, 553–560.

Choi, K.H., Gaynor, J.B., White, K.G., López, C., Bosio, C.M., Karkhoff-Schweizer, R.R., Schweizer, H.P., 2005. A Tn*7*-based broad-range bacterial cloning and expression system. Nat. Methods 2, 443–448.

Choi, K.H., Kumar, A., Schweizer, H.P., 2006. A 10-min method for preparation of highly electrocompetent *Pseudomonas aeruginosa* cells: application for DNA fragment transfer between chromosomes and plasmid transformation. J. Microbiol. Methods 64, 391–397.

Choi, K.H., Schweizer, H.P., 2006. Mini-Tn*7* insertion in bacteria with single *att*Tn*7* sites: example *Pseudomonas aeruginosa*. Nat. Protoc. 1, 153–161.

Cros, A., Alfaro-Espinoza, G., de Maria, A., Wirth, N.T., Nikel, P.I., 2022. Synthetic metabolism for biohalogenation. Curr. Opin. Biotechnol. 74, 180–193.

Crown, S.B., Antoniewicz, M.R., 2012. Selection of tracers for ^{13}C-metabolic flux analysis using elementary metabolite units (EMU) basis vector methodology. Metab. Eng. 14, 150–161.

Daddaoua, A., Krell, T., Alfonso, C., Morel, B., Ramos, J.L., 2010. Compartmentalized glucose metabolism in *Pseudomonas putida* is controlled by the PtxS repressor. J. Bacteriol. 192, 4357–4366.

del Castillo, T., Ramos, J.L., Rodríguez-Herva, J.J., Fuhrer, T., Sauer, U., Duque, E., 2007. Convergent peripheral pathways catalyze initial glucose catabolism in *Pseudomonas putida*: genomic and flux analysis. J. Bacteriol. 189, 5142–5152.

Ebert, B.E., Kurth, F., Grund, M., Blank, L.M., Schmid, A., 2011. Response of *Pseudomonas putida* KT2440 to increased NADH and ATP demand. Appl. Environ. Microbiol. 77, 6597–6605.

Ebrahim, A., Lerman, J.A., Palsson, B.Ø., Hyduke, D.R., 2013. COBRApy: COnstraints-based reconstruction and analysis for Python. BMC Syst. Biol. 7, 74.

Fernández-Cabezón, L., Cros, A., Nikel, P.I., 2019. Evolutionary approaches for engineering industrially-relevant phenotypes in bacterial cell factories. Biotechnol. J. 14, 1800439.

Gambacorta, F.V., Dietrich, J.J., Yan, Q., Pfleger, B.F., 2020. Rewiring yeast metabolism to synthesize products beyond ethanol. Curr. Opin. Chem. Biol. 59, 182–192.

Gatto, L., Gibb, S., Rainer, J., 2021. *MSnbase*, efficient and elegant R-based processing and visualization of raw mass spectrometry data. J. Proteome Res. 20, 1063–1069.

Genee, H.J., Bonde, M.T., Bagger, F.O., Jespersen, J.B., Sommer, M.O.A., Wernersson, R., Olsen, L.R., 2015. Software-supported *USER* cloning strategies for site-directed mutagenesis and DNA assembly. ACS Synth. Biol. 4, 342–349.

Hartmans, S., Smits, J.P., van der Werf, M.J., Volkering, F., de Bont, J.A., 1989. Metabolism of styrene oxide and 2-phenylethanol in the styrene-degrading *Xanthobacter* strain 124X. Appl. Environ. Microbiol. 55, 2850–2855.

He, F., 2011. Bradford protein assay. Bio-Protocol 1, e45.

Hellgren, J., Godina, A., Nielsen, J., Siewers, V., 2020. Promiscuous phosphoketolase and metabolic rewiring enables novel non-oxidative glycolysis in yeast for high-yield production of acetyl-CoA derived products. Metab. Eng. 62, 150–160.

Henard, C.A., Freed, E.F., Guarnieri, M.T., 2015. Phosphoketolase pathway engineering for carbon-efficient biocatalysis. Curr. Opin. Biotechnol. 36, 183–188.

Hõrak, R., Kivisaar, M., 1998. Expression of the transposase gene *tnpA* of Tn*4652* is positively affected by integration host factor. J. Bacteriol. 180, 2822–2829.

Huber, W., von Heydebreck, A., Sültmann, H., Poustka, A., Vingron, M., 2002. Variance stabilization applied to microarray data calibration and to the quantification of differential expression. Bioinformatics 18, S96–S104.

Ilves, H., Hõrak, R., Kivisaar, M., 2001. Involvement of σ^S in starvation-induced transposition of *Pseudomonas putida* transposon Tn*4652*. J. Bacteriol. 183, 5445–5448.

Ishida, N., Suzuki, T., Tokuhiro, K., Nagamori, E., Onishi, T., Saitoh, S., Kitamoto, K., Takahashi, H., 2006. D-Lactic acid production by metabolically engineered *Saccharomyces cerevisiae*. J. Biosci. Bioeng. 101, 172–177.

Karp, P.D., Billington, R., Caspi, R., Fulcher, C.A., Latendresse, M., Kothari, A., Keseler, I. M., Krummenacker, M., Midford, P.E., Ong, Q., Ong, W.K., Paley, S.M., Subhraveti, P., 2019. The BioCyc collection of microbial genomes and metabolic pathways. Briefings Bioinf. 20, 1085–1093.

Kivistik, P.A., Kivisaar, M., Hõrak, R., 2007. Target site selection of *Pseudomonas putida* transposon Tn*4652*. J. Bacteriol. 189, 3918–3921.

Klinke, S., Dauner, M., Scott, G., Kessler, B., Witholt, B., 2000. Inactivation of isocitrate lyase leads to increased production of medium-chain-length poly(3-hydroxyalkanoates) in *Pseudomonas putida*. Appl. Environ. Microbiol. 66, 909–913.

Kohlstedt, M., Wittmann, C., 2019. GC-MS-based ^{13}C metabolic flux analysis resolves the parallel and cyclic glucose metabolism of *Pseudomonas putida* KT2440 and *Pseudomonas aeruginosa* PAO1. Metab. Eng. 54, 35–53.

Kozaeva, E., Volkova, S., Matos, M.R.A., Mezzina, M.P., Wulff, T., Volke, D.C., Nielsen, L. K., Nikel, P.I., 2021. Model-guided dynamic control of essential metabolic nodes boosts acetyl-coenzyme A–dependent bioproduction in rewired *Pseudomonas putida*. Metab. Eng. 67, 373–386.

Krüsemann, J.L., Lindner, S.N., Dempfle, M., Widmer, J., Arrivault, S., Debacker, M., He, H., Kubis, A., Chayot, R., Anissimova, M., Marlière, P., Cotton, C.A.R., Bar-Even, A., 2018. Artificial pathway emergence in central metabolism from three recursive phosphoketolase reactions. FEBS J. 285, 4367–4377.

Ku, J.T., Chen, A.Y., Lan, E.I., 2020. Metabolic engineering design strategies for increasing acetyl-CoA flux. Metabolites 10, 166.

Kutuzova, S., Colaianni, P., Röst, H., Sachsenberg, T., Alka, O., Kohlbacher, O., Burla, B., Torta, F., Schrübbers, L., Kristensen, M., Nielsen, L., Herrgård, M.J., McCloskey, D., 2020. SmartPeak automates targeted and quantitative metabolomics data processing. Anal. Chem. 92, 15968–15974.

Lipmann, F., Tuttle, L.C., 1945. A specific micromethod for the determination of acyl phosphates. J. Biol. Chem. 159, 21–28.

Liu, Q., Yu, T., Li, X., Chen, Y., Campbell, K., Nielsen, J., Chen, Y., 2019. Rewiring carbon metabolism in yeast for high level production of aromatic chemicals. Nat. Commun. 10, 4976.

Lu, X., Liu, Y., Yang, Y., Wang, S., Wang, Q., Wang, X., Yan, Z., Cheng, J., Liu, C., Yang, X., Luo, H., Yang, S., Gou, J., Ye, L., Lu, L., Zhang, Z., Guo, Y., Nie, Y., Lin, J., Li, S., Tian, C., Cai, T., Zhuo, B., Ma, H., Wang, W., Ma, Y., Liu, Y., Li, Y., Jiang, H., 2019. Constructing a synthetic pathway for acetyl-coenzyme A from one-carbon through enzyme design. Nat. Commun. 10, 1378.

Maerker, C., Rohde, M., Brakhage, A.A., Brock, M., 2005. Methylcitrate synthase from *Aspergillus fumigatus*. FEBS J. 272, 3615–3630.

Martínez-García, E., Jatsenko, T., Kivisaar, M., de Lorenzo, V., 2014a. Freeing *Pseudomonas putida* KT2440 of its proviral load strengthens endurance to environmental stresses. Environ. Microbiol. 17, 76–90.

Martínez-García, E., Nikel, P.I., Aparicio, T., de Lorenzo, V., 2014b. *Pseudomonas* 2.0: genetic upgrading of *P. putida* KT2440 as an enhanced host for heterologous gene expression. Microb. Cell Factories 13, 159.

Martínez-García, E., Nikel, P.I., Chavarría, M., de Lorenzo, V., 2014c. The metabolic cost of flagellar motion in *Pseudomonas putida* KT2440. Environ. Microbiol. 16, 291–303.
Martínez-García, E., Goñi-Moreno, A., Bartley, B., McLaughlin, J., Sánchez-Sampedro, L., Pascual del Pozo, H., Prieto Hernández, C., Marletta, A.S., de Lucrezia, D., Sánchez-Fernández, G., Fraile, S., de Lorenzo, V., 2019. *SEVA 3.0*: an update of the Standard European Vector Architecture for enabling portability of genetic constructs among diverse bacterial hosts. Nucleic Acids Res. 48, D1164–D1170.
Matsushita, K., Shinagawa, E., Adachi, O., Ameyama, M., 1979. Membrane-bound D-gluconate dehydrogenase from *Pseudomonas aeruginosa*. Its kinetic properties and a reconstitution of gluconate oxidase. J. Biochem. 86, 249–256.
McVey, A.C., Medarametla, P., Chee, X., Bartlett, S., Poso, A., Spring, D.R., Rahman, T., Welch, M., 2017. Structural and functional characterization of malate synthase G from opportunistic pathogen *Pseudomonas aeruginosa*. Biochemistry 56, 5539–5549.
Mezzina, M.P., Manoli, M.T., Prieto, M.A., Nikel, P.I., 2021. Engineering native and synthetic pathways in *Pseudomonas putida* for the production of tailored polyhydroxyalkanoates. Biotechnol. J. 16, 2000165.
Mutalik, V.K., Guimaraes, J.C., Cambray, G., Lam, C., Christoffersen, M.J., Mai, Q.A., Tran, A.B., Paull, M., Keasling, J.D., Arkin, A.P., Endy, D., 2013. Precise and reliable gene expression *via* standard transcription and translation initiation elements. Nat. Methods 10, 354–360.
Nikel, P.I., de Lorenzo, V., 2013. Engineering an anaerobic metabolic regime in *Pseudomonas putida* KT2440 for the anoxic biodegradation of 1,3-dichloroprop-1-ene. Metab. Eng. 15, 98–112.
Nikel, P.I., Chavarría, M., Fuhrer, T., Sauer, U., de Lorenzo, V., 2015. *Pseudomonas putida* KT2440 strain metabolizes glucose through a cycle formed by enzymes of the Entner-Doudoroff, Embden-Meyerhof-Parnas, and pentose phosphate pathways. J. Biol. Chem. 290, 25920–25932.
Nikel, P.I., Chavarría, M., Danchin, A., de Lorenzo, V., 2016a. From dirt to industrial applications: *Pseudomonas putida* as a Synthetic Biology *chassis* for hosting harsh biochemical reactions. Curr. Opin. Chem. Biol. 34, 20–29.
Nikel, P.I., Pérez-Pantoja, D., de Lorenzo, V., 2016b. Pyridine nucleotide transhydrogenases enable redox balance of *Pseudomonas putida* during biodegradation of aromatic compounds. Environ. Microbiol. 18, 3565–3582.
Nikel, P.I., Fuhrer, T., Chavarría, M., Sánchez-Pascuala, A., Sauer, U., de Lorenzo, V., 2021. Reconfiguration of metabolic fluxes in *Pseudomonas putida* as a response to sub-lethal oxidative stress. ISME J. 15, 1751–1766.
Nitschel, R., Ankenbauer, A., Welsch, I., Wirth, N.T., Massner, C., Ahmad, N., McColm, S., Borges, F., Fotheringham, I., Takors, R., Blombach, B., 2020. Engineering *Pseudomonas putida* KT2440 for the production of isobutanol. Eng. Life Sci. 20, 148–159.
Nogales, J., Mueller, J., Gudmundsson, S., Canalejo, F.J., Duque, E., Monk, J., Feist, A. M., Ramos, J.L., Niu, W., Palsson, B.Ø., 2020. High-quality genome-scale metabolic modelling of *Pseudomonas putida* highlights its broad metabolic capabilities. Environ. Microbiol. 22, 255–269.
Orsi, E., Claassens, N.J., Nikel, P.I., Lindner, S.N., 2021. Growth-coupled selection of synthetic modules to accelerate cell factory development. Nat. Commun. 12, 5295.
Orsi, E., Claassens, N.J., Nikel, P.I., Lindner, S.N., 2022. Optimizing microbial networks through metabolic bypasses. Biotechnol. Adv. 60, 108035.
Orth, J.D., Thiele, I., Palsson, B.Ø., 2010. What is flux balance analysis? Nat. Biotechnol. 28, 245–248.
Patel, M.S., Nemeria, N.S., Furey, W., Jordan, F., 2014. The pyruvate dehydrogenase complexes: structure-based function and regulation. J. Biol. Chem. 289, 16615–16623.
Pecoraro, V., Zerulla, K., Lange, C., Soppa, J., 2011. Quantification of ploidy in proteobacteria revealed the existence of monoploid, (mero-)oligoploid and polyploid species. PLoS One 6, e16392.
Pedersen, B.H., Gurdo, N., Johansen, H.K., Molin, S., Nikel, P.I., La Rosa, R., 2021. High-throughput dilution-based growth method enables time-resolved exo-metabolomics of *Pseudomonas putida* and *Pseudomonas aeruginosa*. Microb. Biotechnol. 14, 2214–2226.
Platt, R., Drescher, C., Park, S.K., Phillips, G.J., 2000. Genetic system for reversible integration of DNA constructs and *lacZ* gene fusions into the *Escherichia coli* chromosome. Plasmid 43, 12–23.
Poblete-Castro, I., Becker, J., Dohnt, K., Martins dos Santos, V.A.P., Wittmann, C., 2012. Industrial biotechnology of *Pseudomonas putida* and related species. Appl. Microbiol. Biotechnol. 93, 2279–2290.
Qin, N., Li, L., Ji, X., Li, X., Zhang, Y., Larsson, C., Chen, Y., Nielsen, J., Liu, Z., 2020. Rewiring central carbon metabolism ensures increased provision of acetyl-CoA and NADPH required for 3-OH-propionic acid production. ACS Synth. Biol. 9, 3236–3244.
Qiu, Y.Q., 2013. KEGG pathway database. In: Dubitzky, W., Wolkenhauer, O., Cho, K.-H., Yokota, H. (Eds.), Encyclopedia of Systems Biology. Springer New York, New York, NY, pp. 1068–1069.
Rennig, M., Mundhada, H., Wordofa, G.G., Gerngross, D., Wulff, T., Worberg, A., Nielsen, A.T., Nørholm, M.H.H., 2019. Industrializing a bacterial strain for L-serine production through translation initiation optimization. ACS Synth. Biol. 8, 2347–2358.
Ritchie, M.E., Phipson, B., Wu, D., Hu, Y., Law, C.W., Shi, W., Smyth, G.K., 2015. *Limma* powers differential expression analyses for RNA-sequencing and microarray studies. Nucleic Acids Res. 43, e47.
Sambrook, J., Russell, D.W., 2001. Molecular Cloning: a Laboratory Manual. Cold Spring Harbor Laboratory, Cold Spring Harbor.
Sandberg, T.E., Salazar, M.J., Weng, L.L., Palsson, B.Ø., Feist, A.M., 2019. The emergence of adaptive laboratory evolution as an efficient tool for biological discovery and industrial biotechnology. Metab. Eng. 56, 1–16.
Scardovi, V., Trovatelli, L.D., 1965. The fructose-6-phosphate shunt as peculiar pattern of hexose degradation in the genus *Bifidobacterium*. Ann. Microbiol. Enz. 15, 19–29.
Schuiki, I., Daum, G., 2009. Phosphatidylserine decarboxylases, key enzymes of lipid metabolism. IUBMB Life 61, 151–162.
Shi, L., Tu, B.P., 2015. Acetyl-CoA and the regulation of metabolism: mechanisms and consequences. Curr. Opin. Cell Biol. 33, 125–131.
Sievers, M., Stöckli, M., Teuber, M., 1997. Purification and properties of citrate synthase from *Acetobacter europaeus*. FEMS Microbiol. Lett. 146, 53–58.
Song, C.W., Park, J.M., Chung, S.C., Lee, S.Y., Song, H., 2019. Microbial production of 2,3-butanediol for industrial applications. J. Ind. Microbiol. Biotechnol. 46, 1583–1601.
Strimmer, K., 2008. *fdrtool*: a versatile R package for estimating local and tail area-based false discovery rates. Bioinformatics 24, 1461–1462.
Swain, P.S., Stevenson, K., Leary, A., Montano-Gutiérrez, L.F., Clark, I.B.N., Vogel, J., Pilizota, T., 2016. Inferring time derivatives including cell growth rates using Gaussian processes. Nat. Commun. 7, 13766.
Tittmann, K., 2014. Sweet siblings with different faces: the mechanisms of FBP and F6P aldolase, transaldolase, transketolase and phosphoketolase revisited in light of recent structural data. Bioorg. Chem. 57, 263–280.
Torrontegui, D., Díaz, R., Cánovas, J.L., 1976. The uptake of 2-ketogluconate by *Pseudomonas putida*. Arch. Microbiol. 110, 43–48.
Udaondo, Z., Ramos, J.L., Segura, A., Krell, T., Daddaoua, A., 2018. Regulation of carbohydrate degradation pathways in *Pseudomonas* involves a versatile set of transcriptional regulators. Microb. Biotechnol. 11, 442–454.
Vadali, R.V., Bennett, G.N., San, K.Y., 2004. Cofactor engineering of intracellular CoA/acetyl-CoA and its effect on metabolic flux redistribution in *Escherichia coli*. Metab. Eng. 6, 133–139.
Valgepea, K., Adamberg, K., Nahku, R., Lahtvee, P.J., Arike, L., Vilu, R., 2010. Systems biology approach reveals that overflow metabolism of acetate in *Escherichia coli* is triggered by carbon catabolite repression of acetyl-CoA synthetase. BMC Syst. Biol. 4, 166.
van Duuren, J.B., Puchałka, J., Mars, A.E., Bücker, R., Eggink, G., Wittmann, C., Martins dos Santos, V.A.P., 2013. Reconciling *in vivo* and *in silico* key biological parameters of *Pseudomonas putida* KT2440 during growth on glucose under carbon-limited condition. BMC Biotechnol. 13, 93.
Volke, D.C., Nikel, P.I., 2018. Getting bacteria in shape: synthetic morphology approaches for the design of efficient microbial cell factories. Adv. Biosyst. 2, 1800111.
Volke, D.C., Calero, P., Nikel, P.I., 2020a. *Pseudomonas putida*. Trends Microbiol. 28, 512–513.
Volke, D.C., Friis, L., Wirth, N.T., Turlin, J., Nikel, P.I., 2020b. Synthetic control of plasmid replication enables target- and self-curing of vectors and expedites genome engineering of *Pseudomonas putida*. Metab. Eng. Commun. 10, e00126.
Volke, D.C., Olavarría, K., Nikel, P.I., 2021. Cofactor specificity of glucose-6-phosphate dehydrogenase isozymes in *Pseudomonas putida* reveals a general principle underlying glycolytic strategies in bacteria. mSystems 6, e00014. -21.
Volke, D.C., Martino, R.A., Kozaeva, E., Smania, A.M., Nikel, P.I., 2022. Modular (de) construction of complex bacterial phenotypes by CRISPR/nCas9-assisted, multiplex cytidine base-editing. Nat. Commun. 13, 3026.
Wang, Q., Xu, J., Sun, Z., Luan, Y., Li, Y., Wang, J., Liang, Q., Qi, Q., 2019. Engineering an *in vivo* EP-bifido pathway in *Escherichia coli* for high-yield acetyl-CoA generation with low CO_2 emission. Metab. Eng. 51, 79–87.
Wang, Y., Zhou, S., Li, R., Liu, Q., Shao, X., Zhu, L., Kang, M.K., Wei, G., Kim, S.W., Wang, C., 2022. Reassessing acetyl-CoA supply and NADPH availability for mevalonate biosynthesis from glycerol in *Escherichia coli*. Biotechnol. Bioeng. 119, 2868–2877.
Weimer, A., Kohlstedt, M., Volke, D.C., Nikel, P.I., Wittmann, C., 2020. Industrial biotechnology of *Pseudomonas putida*: advances and prospects. Appl. Microbiol. Biotechnol. 104, 7745–7766.
Wenk, S., Yishai, O., Lindner, S.N., Bar-Even, A., 2018. An engineering approach for rewiring microbial metabolism. Methods Enzymol. 608, 329–367.
Wirth, N.T., Kozaeva, E., Nikel, P.I., 2020. Accelerated genome engineering of *Pseudomonas putida* by I-*Sce*I–mediated recombination and CRISPR-Cas9 counterselection. Microb. Biotechnol. 13, 233–249.
Wirth, N.T., Nikel, P.I., 2021. Combinatorial pathway balancing provides biosynthetic access to 2-fluoro-*cis,cis*-muconate in engineered *Pseudomonas putida*. Chem Catal 1, 1234–1259.
Worsey, M.J., Williams, P.A., 1975. Metabolism of toluene and xylenes by *Pseudomonas putida* (*arvilla*) mt-2: evidence for a new function of the TOL plasmid. J. Bacteriol. 124, 7–13.
Wu, T., Hu, E., Xu, S., Chen, M., Guo, P., Dai, Z., Feng, T., Zhou, L., Tang, W., Zhan, L., Fu, X., Liu, S., Bo, X., Yu, G., 2021. *clusterProfiler* 4.0: a universal enrichment tool for interpreting omics data. Innovation 2, 100141.
Wu, X., Monchy, S., Taghavi, S., Zhu, W., Ramos, J.L., van der Lelie, D., 2011. Comparative genomics and functional analysis of niche-specific adaptation in *Pseudomonas putida*. FEMS Microbiol. Rev. 35, 299–323.
Yang, D., Park, S.Y., Park, Y.S., Eun, H., Lee, S.Y., 2020. Metabolic engineering of *Escherichia coli* for natural product biosynthesis. Trends Biotechnol. 38, 745–765.
Young, J.D., 2014. *INCA*: a computational platform for isotopically non-stationary metabolic flux analysis. Bioinformatics 30, 1333–1335.
Zhu, L., Zhang, J., Yang, J., Jiang, Y., Yang, S., 2022. Strategies for optimizing acetyl-CoA formation from glucose in bacteria. Trends Biotechnol. 40, 149–165.
Zobel, S., Benedetti, I., Eisenbach, L., de Lorenzo, V., Wierckx, N.J.P., Blank, L.M., 2015. Tn*7*-Based device for calibrated heterologous gene expression in *Pseudomonas putida*. ACS Synth. Biol. 4, 1341–1351.